Energy & Environmental Science

ROYAL SOCIETY OF CHEMISTRY

ANALYSIS

Cite this: *Energy Environ. Sci.*, 2016, **9**, 803

Opportunities to improve the net energy performance of photoelectrochemical water-splitting technology†

Roger Sathre,*[ab] Jeffery B. Greenblatt,*[ab] Karl Walczak,[ac] Ian D. Sharp,[ad] John C. Stevens,[ac] Joel W. Ager, III[ac] and Frances A. Houle[ad]

Received 5th October 2015,
Accepted 19th February 2016

DOI: 10.1039/c5ee03040d

www.rsc.org/ees

The hydrogen energy provided by solar-driven photoelectrochemical (PEC) water splitting must be greater than the energy used to produce and operate the technology, as a fundamental system requirement to enable energetic benefits to society. PEC H_2 production will require significant advances from both basic scientific research and applied technology development, prior to manufacturing and field deployment. To identify opportunities and priorities, here we use prospective life cycle system modeling to investigate the net-energy significance of six characteristics describing the PEC life cycle: (1) embodied energy of active cell materials, (2) embodied energy of inactive module materials, (3) energy intensity of active cell fabrication, (4) energy intensity of PEC module assembly, (5) initial energy use for production of balance-of-system (BOS), and (6) ongoing energy use for operation and end-of-life of BOS. We develop and apply a system model describing material and energy flows during the full life cycle of louvered thin-film PEC cells and their associated modules and BOS components. We find that fabrication processes for the PEC cells, especially the thin-film deposition of active cell materials, are important drivers of net energy performance. Nevertheless, high solar-to-hydrogen (STH) conversion efficiency and long cell life span are primary design requirements for PEC systems, even if such performance requires additional energy and material inputs for production and operation. We discuss these and other system dynamics, and highlight pathways to improve net energy performance.

Broader context

Long-term human development will require environmentally benign renewable energy supply systems, to replace our current dependence on fossil fuels. The net energy of such systems, *i.e.* the renewable energy harvested minus the energy used to build and operate the system, must be substantially positive to enable energetic benefits to society. Using prospective life cycle modeling, we assess the net energy balance of large-scale hydrogen fuel production *via* solar driven photoelectrochemical water splitting technology. We identify the factors that strongly improve net energy performance, including high solar-to-hydrogen conversion efficiency, long life span of the water splitting device, and low energy use for manufacturing the device. Solar fuels research should focus on achieving success in these factors, to enable future deployment of solar fuel systems that provide meaningful energy services to society.

1. Introduction

A transition from fossil to renewable energy sources is required for reasons of environmental quality and energy security.[1] Globally, we are heavily dependent on fossil fuels for transportation, electricity, heat, and other energy services. The three types of fossil fuels—coal, oil and natural gas—currently supply about 82% of all global primary energy use.[2] Combustion of fossil fuels leads to a range of detrimental impacts, including climate change[3] and human health effects.[4] Furthermore, as fossil fuels are formed largely from decayed organisms that were alive hundreds of millions of years ago, they are non-renewable over time scales of interest. Long-term human development will thus require a transition to renewable energy sources.

Because most renewable energy resources are diffuse (such as solar and wind), the capture area needed to harness a significant energy supply must be extensive. Specifically for photovoltaic (PV)

[a] *Joint Center for Artificial Photosynthesis, Berkeley, CA, USA. E-mail: roger@transformativetechnologies.org, jbgreenblatt@lbl.gov*
[b] *Energy Analysis and Environmental Impacts Division, Lawrence Berkeley National Laboratory, Berkeley, CA, USA*
[c] *Materials Sciences Division, Lawrence Berkeley National Laboratory, Berkeley, CA, USA*
[d] *Chemical Sciences Division, Lawrence Berkeley National Laboratory, Berkeley, CA, USA*

† Electronic supplementary information (ESI) available. See DOI: 10.1039/c5ee03040d

power, Ong *et al.*[5] calculated that the average capacity-weighted direct land use required by US PV installations is 1.3 ha per GW h per year. At this land use rate, a PV facility would require about 100 km^2 of land area to produce the same amount of electricity made by a 1 GW fossil fuel-fired plant operating with a 90% capacity factor. The extensive infrastructure needed over such a large area comes at a relatively high energy cost, leading to long energy pay-back times and modest life-cycle energy returns on investment for renewable energy facilities.[6] This challenge is compounded by the intermittent nature of renewable energy supply, and the difficulty of storing large amounts of PV electricity for use over diurnal and annual supply cycles.

Photoelectrochemical (PEC) water splitting devices are intended to directly convert solar radiation into hydrogen, a storable fuel, at relatively high energy conversion efficiencies. If successfully deployed, a future PEC device could overcome the challenge of intermittency of solar resources, by directly producing a fuel that can be stored and used upon demand. Hydrogen offers many of the same advantages as hydrocarbon fuels but without the CO_2 emissions upon combustion. For vehicle transportation, hydrogen-powered fuel cells overcome many of the current limitations of battery technology such as range, weight and cost (though ongoing research and economies of scale may further improve battery characteristics.) Solar-to-hydrogen (STH) efficiency is a commonly used performance metric of PEC devices. As defined by Chen *et al.*,[7] STH efficiency compares the Gibbs free energy of the hydrogen produced by a device under zero external bias conditions, to the solar radiation incident on the device exposed to solar AM1.5G illumination.

While STH efficiency is an important metric for benchmarking and comparing device-level performance,[8,9] it does not, by itself, indicate the overall energetic utility of a PEC technology, because it does not consider essential non-solar energy inputs to the system. These technological energy inputs, *e.g.* for material supply, manufacturing, operations, and end-of-life management of the system, may be significant. Appropriate metrics for system-level performance may be obtained through net energy analysis (Fig. 1). The net energy of a system is the energy available for societal use, after subtracting the energy required to create and operate the technology. If the energy inputs to the system approach the usable renewable energy harvested by the system, its contribution to sustaining societal wellbeing becomes negligible.

In previous studies, we have analyzed various aspects of net energy performance of PEC systems. Zhai *et al.*[10] employed an innovative hybrid (bottom-up top-down) modeling approach to assess the device-level net energy balance of a silicon microwire PEC cell. Sathre *et al.*[11] added the balance-of-system (BOS) and end-of-life (EOL) energy effects to this cell design, producing the first system-wide net energy assessment of large-scale PEC hydrogen production. In the present analysis we build upon these frameworks, to enable broader research questions. In this paper we introduce: (1) an innovative PEC cell and module architecture, with emphasis on large-scale manufacturability and operability; (2) more advanced analytical methodology, *e.g.* a novel method for estimating the embodied energy of a wide range of thin-film materials; (3) more refined technical design process, *e.g.* a rational reduction of materials used in PEC modules; (4) more thorough analysis of the energy implications of thin-film manufacture, considering a range of material combinations and deposition technologies.

We use prospective life cycle system modeling techniques to estimate the energy flows during the manufacture, operation and EOL of an eventual large-scale PEC water splitting facility and its supply chain, and we chart the opportunities for improving performance. Our goal is to identify key relationships and sensitivities across a range of materials and processes, rather than to find a single "correct" result. The early-stage life cycle modeling presented here is intended to generate knowledge to inform decisions made by materials scientists (*e.g.* performance targets for laboratory research), process engineers (*e.g.* design parameters for system scale-up), and policy makers (*e.g.* eventual net energy potentials of PEC systems). Combined with techno-economic analysis (*e.g.* ref. 12), it provides a more robust basis for early-stage decision-making.

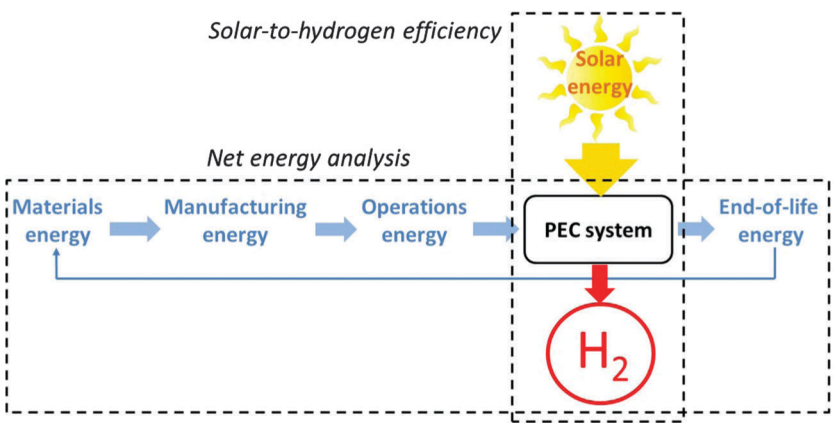

Fig. 1 Solar-to-hydrogen efficiency compares the solar energy incident on a PEC cell to the chemical energy of the produced hydrogen. Net energy analysis compares the total technological energy inputs to the system (for material supply, manufacturing, operations, and end-of-life management) to the chemical energy of the produced hydrogen.

2. Methods

2.1 Modeling framework

Prospective life cycle system modeling is a method combining scenario analysis with consequential life cycle assessment (LCA), to evaluate the potential impacts of technologies and infrastructure systems that are not yet operating at commercial scale. It is intended to provide early-stage insights on opportunities and constraints of emerging technologies, to guide basic research toward effective innovation.

We begin the analysis by assuming a functional PEC technology with a given performance level. We then conduct a preliminary engineering design of a hypothetical large-scale PEC water splitting facility, including BOS. We then estimate energy requirements for materials, manufacturing, operation, and decommissioning of the facility. This provides us with information needed to calculate several net energy metrics describing the performance of the system. Furthermore, we apply this method using a range of plausible parametric values to identify sensitivities and quantify uncertainties. Overall, we seek opportunities to improve the life cycle net energy performance of the technology.

We develop and apply a prospective life cycle system model describing system-wide energy flows associated with a hypothetical utility-scale PEC energy facility with H_2 production equivalent to 1 GW annual average (1 GW higher heating value (HHV) annual average = 610 t H_2 per day). The 1 GW hydrogen production facility is configured on five hierarchical levels: cells, modules, panels, fields, and facility. The two smallest levels, the cell and module, are described in Section 2.2. The remaining three levels comprise the BOS and are described in Section 2.3. In particular, we investigate the significance of six key energy characteristics of PEC systems:

(1) Embodied energy of active cell materials (semiconductors, catalysts, transparent conductive oxides (TCO), conductive substrate, protective layers, electrolyte, and membrane materials)

(2) Embodied energy of inactive module materials (window, back cover, frame, and ribs)

(3) Energy intensity of active cell fabrication (thin-film deposition processes and membrane manufacture)

(4) Energy intensity of inactive module fabrication (cell and module assembly)

(5) Initial energy use for production of balance-of-system (BOS) components

(6) Ongoing energy use for operation and end-of-life of BOS components

The first two characteristics describe embodied energy of cell and module material supply, which account for energy used for extraction, primary processing, and transportation of materials to the PEC factory gate. The next two characteristics describe energy intensity of fabrication processes within the factory to produce finished PEC cells and modules. The final two characteristics account for the energy use by the BOS during production, operation and end-of-life of the facility. We quantify each of these characteristics in units of MJ of primary energy use per m^2 of active cell area. Together, these six characteristics comprehensively include energy use during the full life cycle of the technology. With reference to Fig. 1, characteristics 1 and 2 correspond to materials energy, characteristics 3, 4 and 5 correspond to manufacturing energy, and characteristic 6 corresponds to operations and end-of-life energy.

Our system model includes base-case values for each of the six characteristics, as well as high energy input and low energy input values corresponding to other possible configurations of a future large-scale physical system. The modeled high energy input, base case, and low energy input characteristics are described in Table 1. We conduct a sensitivity analysis by varying individual parameters from their base case values to their low input and high input values.

In addition to the six life cycle system characteristics, we evaluate the effects on net energy of varying assumptions of cell performance, considering two key performance parameters: the service life span of the cells in use, and the solar-to-hydrogen conversion efficiency of the cells. Our base-case analysis assumes a cell life span of 10 years, and STH efficiency of 10%. We vary the life span between five and 20 years, and the STH efficiency between 5% and 20%. Due to paucity of data, we are unable to quantitatively link the variations in cell production energy and cell performance, though we conduct exploratory modeling investigations. This model can be refined as laboratory research and industrial capabilities advance, to provide convergence to realistic technology performance. We assume that cell performance degrades linearly over time, with replacement occurring when STH efficiency falls to 80% of its original value. In our modeling this is characterized by a simple degradation factor, such that the average H_2 production over the life span of a cell corresponds to 90% of the nominal STH efficiency. We further assume 10% solar transmittance loss due to the combined effects of absorption, scattering and reflection by surface dust, encapsulation material, and electrolyte.

Across a range of values for the six system characteristics and two performance parameters, we calculate three net energy metrics. The life cycle primary energy balance describes how much usable net energy the facility provides to society during its lifespan. In units of PJ, it is calculated as the total energy output minus the total energy input:

$$\text{Energy balance} = \{T \times E_H\} - \{E_P + (T \times E_o) + E_D\} \quad (1)$$

where T = service life of the facility (years); E_H = energy (HHV) in hydrogen produced in 1 year (PJ per year); E_P = energy used to produce the facility (PJ); E_O = energy used to operate the facility for 1 year (PJ per year); E_D = energy used to decommission the facility (PJ).

The energy return on energy invested (EROEI, sometimes denoted as EROI) describes how much usable energy the facility will deliver, relative to its required energy inputs. A value without units, it is calculated as the total energy output divided by the total energy input:

$$\text{EROEI} = \frac{T \times E_H}{E_P + (T \times E_O) + E_D} \quad (2)$$

The energy payback time describes how long the facility must operate for it to deliver the H_2 equivalent of the energy required

Table 1 Summary description of high energy input, base case, and low energy input characteristics of active cell, inactive module, and BOS components

	High energy input	Base case	Low energy input
(1) Active cell materials	• 250 nm GaAs photoanode • 250 nm InGaP photocathode • 120 nm TiO_2 protective layer • 1 nm Pt HER catalyst • 1 nm IrO_x OER catalyst • 100 nm ITO TCO layer • 20% material utilization • 2 : 1 precursor energy • 0.2 mm stainless steel substrate • 70 μm membrane • Electrolyte	• 250 nm a-Si photoanode • 250 nm $BiVO_4$ photocathode • 60 nm TiO_2 protective layer • 1 nm Pt HER catalyst • 1 nm IrO_x OER catalyst • 50 nm FTO TCO layer • 50% material utilization • 1 : 1 precursor energy • 0.1 mm stainless steel substrate • 50 μm membrane • Electrolyte	• 250 nm a-Si photoanode • 250 nm Fe_2O_3 photocathode • 30 nm TiO_2 protective layer • 1 nm Fe_3P HER catalyst • 1 nm $NiFeO_x$ OER catalyst • 10 nm FTO TCO layer • 80% material utilization • 0.5 : 1 precursor energy • 0.05 mm stainless steel substrate • 30 μm membrane • Electrolyte
(2) Inactive module materials	• 2 × 3 mm glass • Large PVC frame • PVC support ribs	• 2 × 2 mm glass • Medium PVC frame • PVC support ribs	• 2 × 1 mm glass • Small PVC frame • PVC support ribs
(3) Active cell fabrication	Current typical thin-film coating	Current state-of-the-art inline thin-film coating	Solution coating at atmospheric pressure and room temperature
(4) Inactive module fabrication	Base-case × 200%	From Zhai *et al.*[10]	Base-case × 50%
(5) Initial BOS production	Upper 90% confidence interval from Monte Carlo modeling	Adapted from Sathre *et al.*,[11] see text	Lower 90% confidence interval from Monte Carlo modeling
(6) BOS operation and EOL	Upper 90% confidence interval from Monte Carlo modeling	Adapted from Sathre *et al.*,[11] see text	Lower 90% confidence interval from Monte Carlo modeling

for its manufacturing, construction, and decommissioning. Note that energy payback time is not a life cycle metric as it does not consider the energy that continues to be delivered after the payback time is reached; the equation does not include the variable T, the facility service life. In units of years, energy payback time is calculated as the fixed energy inputs divided by the annual net energy output under full-scale continuous operation:

$$\text{Energy Payback Time} = \frac{E_P + E_D}{E_H - E_O} \quad (3)$$

2.2 Photoelectrochemical cell and module

There are a number of potential configurations for PEC cells and a number of different ways they could be classified. For example, they can be classified by their electrochemical architecture, the type and phase of reactants that they use, the products they generate, as wired or wireless devices, or some combination of these characteristics. A more complete description of various solar fuel-harvesting devices is given by Nielander *et al.*[13]

Wired devices are physically integrated, while maintaining chemical isolation between all parts of the photovoltaic cells and the electrolyte (*e.g.* ref. 14), or can allow contact between the electrolyte and the anodic or cathodic portion of a photovoltaic cell, while performing the corresponding cathodic or anodic reactions, respectively, on a separate wired electrode (*e.g.* ref. 15). Wireless devices perform electrochemistry directly on the photovoltaic cell's surfaces, either with or without some layer to protect the active semiconductor material from the chemical reactions (*e.g.* ref. 16). A more comprehensive list of lab-demonstrated wired and wireless hydrogen-producing devices is presented by Ager *et al.*,9 which details notable demonstrated hydrogen-producing PECs. Within the wireless architecture, devices can be additionally characterized by the photoelectrode architecture. There are devices that use planar photoelectrodes,[17] ones that use suspensions of particulates to perform co-evolution of hydrogen and oxygen,[12] and devices whose photoelectrodes are comprised of microwires.[18] The distinction between wired and wireless devices is likely to be small in the context of a net energy analysis because of the small energy cost of wires, assuming that the manufacturing processes are similar for separate and integrated electrodes. The potential benefits in operational lifespan may be more significant. Additionally, many wireless devices are effectively wired due to their use of an ohmic contact rather than a semiconductor–liquid junction.

PECs can additionally be classified by the type and phase of the input reactant they use. Most wireless and wired devices use liquid water as a solvent to form an aqueous electrolyte that is in contact with the electrodes.[14–18] Typically, the solute in the electrolyte is a strong acid or base that confers conductivity to the electrolyte to enable ion transport. In contrast, some PECs can operate using water vapor. The latter devices employ an ion conduction membrane in place of an aqueous medium in order to conduct protons or hydroxyl ions from the anode to the cathode. Possible ways to design such vapor-fed devices are described by Xiang *et al.*,[19] and experimental demonstrations are described by Modestino *et al.*[20]

Another way to classify PECs is by what products are generated in the cell. All of the demonstrated devices cited above generate hydrogen from water splitting. Electrochemically speaking, water splitting is easier to accomplish than reduction

of carbon dioxide to produce hydrocarbon fuels.[21] However, if a low overpotential catalyst were developed, this difference would be reduced. There are transport limits for carbon dioxide reduction reaction, but use of gas diffusion electrodes and/or high pressure can address these. There are several recent demonstrations of no-bias solar-driven carbon dioxide reduction (*e.g.* ref. 22 and 23).

In this analysis, we consider a planar wireless device for water splitting in an aqueous electrolyte. Fig. 2 shows cross-sections of the studied cell and module assembly at different scales. The overall module appears similar to a dual pane window with dimensions of 1 m × 1.2 m and thickness of 11 mm. A ribbed PVC frame is laminated between the glass panes and supports the louvered active cell assembly. Active thin-film layer stacks are angled within the louvered cell geometry, with a membrane mounted vertically in the structure such that it does not significantly reduce the illuminated active area.[16] The oxygen and hydrogen evolution reactions are performed on opposite faces of the active device stack and the ion-exchange membranes separate the hydrogen and oxygen product gases. The thin-film device layers are also shown (not to scale) in Fig. 2, and include a tandem photoabsorber, transparent conductive oxide (TCO) layer, protective anti-corrosion layer, and electrocatalyst layers for the oxygen-evolution reaction (OER) and hydrogen-evolution reaction (HER).

2.2.1. Embodied energy of active cell materials. This characteristic includes energy used for extraction, primary processing and transportation to the cell factory gate for the active device materials or their precursors. These materials include semiconductors, catalysts, transparent conductive oxide (TCO), conductive substrate, electrolyte, and membranes. Within the louvered geometry, we consider a generic electrochemical design with a range of potential active materials. Embodied energy describes the primary energy used for extraction, processing and transportation of materials. It does not include the energy used for thin film deposition within the PEC cell factory, which is described in Section 2.2.3. Is also does not consider performance variations between materials in, for example, deposition energy intensity, product yield, STH efficiency, and cell life span.

Robustly quantifying the embodied energy of a diverse range of chemical compounds remains a challenge for the LCA community. Although standard life cycle inventory (LCI) databases (*e.g.* Ecoinvent, USLCI) contain embodied energy estimates for thousands of common commodity elements and compounds, they do not include data for tens of thousands of other specialty chemicals that are produced and used in smaller amounts. Many of the final or precursor materials of the thin films studied here are not represented in LCI databases or related literature. To overcome this challenge, in this analysis we use a simplified and generic approach. We estimate the embodied energy of precursor materials for thin film deposition using eqn (4):

$$\text{Thin film material energy} = \sum_{\text{layers}}^{i} \sum_{\text{elements}}^{j} \frac{M_s \times E_s \times R_p}{F_m} \quad (4)$$

We sum over i layers of thin film, each containing up to j elements, and we quantify the embodied energy of each element

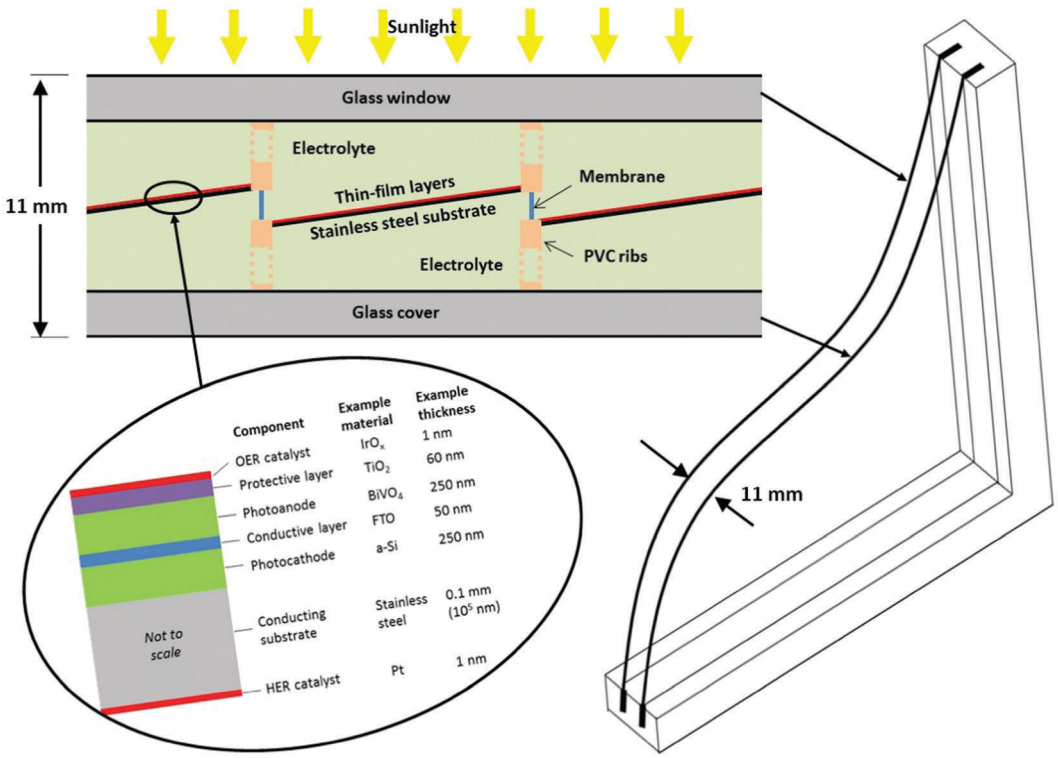

Fig. 2 Cross-sections of PEC cell and module, including dual pane glass module encapsulation (right), louvered active cell configuration (top left), and thin-film layers of active cell materials (bottom left).

based on 4 factors. The factor M_s is the specific mass, and quantifies the mass of the element per square meter of thin film layer [kg m^{-2}]. The factor E_s is the specific embodied primary energy of the refined element, *i.e.* the total energy needed to extract, process, transport and refine a unit mass of the element [MJ kg^{-1}]. The factor R_p is the ratio of the embodied energy of the refined element to that of the precursor material used in the deposition process, both measured per unit mass of the element. The factor F_m is the material utilization efficiency, and quantifies the mass of the element in the final thin film product per unit mass of the element in precursor materials delivered to the factory gate. R_p and F_m are both ratios without units, thus eqn (4) expresses the embodied energy of active cell materials in units of MJ of primary energy per m^2 of active cell area.

The specific mass M_s of materials deposited in each thin-film layer is calculated based on the layer thickness and the material density. Details on a range of thin film layers are listed in Table S1 of the ESI.† In our base case we assume a 250 nm thickness for the photoanode and the photocathode, 200 nm thickness for the TCO layer, 60 nm thickness for the TiO_2 protective layer, and 1 nm thickness for the HER and OER catalysts. Within each deposited compound, we determine the mass of each element based on stoichiometry of the compound and atomic masses of the elements.

The embodied energy E_s of most refined elements is available from standard LCI databases. We base our calculations largely on embodied energy data from the Ecoinvent database,[24] supplemented with data from Nuss & Eckelman.[25] The embodied energy of an element will likely depend on its purity; processing energy requirements increase significantly as the purity increases and allowable contaminant level decreases.[26] Processes used to attain high purity materials include distillation, adsorption, ion exchange, filtration, and crystallization. In this analysis we use the default purity levels used in the Ecoinvent database,[24] which typically represent the purest form of the element widely used in representative industries.[27]

In some thin film deposition processes, the final deposited material is the same as the process raw material. For example, magnetron sputtering targets of a particular metal are used to deposit a thin film of the same metal. In many cases, however, the material composition of the finished thin film differs from the precursor materials used in the deposition process. For example, a TiO_2 protective layer may be applied from molecular precursors such as titanium isopropoxide or tetrakis(dimethylamido)titanium, using atomic layer deposition (ALD). Materials such as InP that are deposited by MOCVD are typically formed from other precursors, *e.g.* trimethyl indium and phosphine. Atmospheric pressure depositions also use non-elemental or oxide precursors; *e.g.* $BiVO_4$ can be deposited from bismuth nitrate and vanadium acetylacetonate. Thin films of indium tin oxide (ITO) can be formed by spray pyrolysis using $InCl_3$ and $SnCl_4$ precursors, and fluorine doped tin oxide (FTO) using $SnCl_4$ and NH_4F precursors. Amorphous silicon is typically deposited from a mixture of hydrogen and silane using plasma-enhanced chemical vapor deposition (PECVD). We account for this ambiguity with a factor R_p expressing the ratio of the embodied energy of the refined element to that of the precursor materials used in the thin film deposition process, both measured per unit mass of the element. We assume a base-case value of 1.0 for this ratio, with a range from 2.0 to 0.5. These values are justified and discussed in Section S2 of the ESI.†

A final factor affects the embodied energy of cell material supply: the material utilization efficiency F_m expresses the mass of the element in the final thin film, per unit mass of the element in precursor materials delivered to the factory gate. This factor is determined by the material application yield (the percent of raw material element that is contained in finished thin films, the balance being wasted during the thin-film deposition process), the factory product yield (the percent of deposited thin film area in finished PEC modules, the balance being defective products), and the material recycling rate (the percent of waste element generated from material application and factory product yields that is recovered and reused). In practice, the material utilization efficiency will vary between deposition processes and materials, with gaseous precursor chemical reaction processes being the least material efficient and electrodeposition being the most material efficient. For example, Kreiger *et al.*[28] reported silane utilization of only 15% in conventional amorphous silicon deposition, but up to 83% utilization when silane is recycled instead of flared. Fthenakis[29] reported material utilization of only 34% for indium deposited by co-evaporation during commercial CIGS thin film production, but up to 90% utilization *via* electrodeposition or by recovering residuals from vapor deposition. Alsema[30] reported a material utilization efficiency of 30–40% for sputtering deposition of TCO layers. Zweibel[31] reported material utilization efficiencies of various thin film deposition processes: 10–25% for germanium applied as germane gas during amorphous silicon deposition, 50% for indium during CIGS evaporation deposition, 75% for indium during CIGS sputtering deposition, 75% for CdTe powder during commercial CdTe sublimation deposition, and 95% for tellurium during electrodeposition of CdTe thin films. Across this diversity of materials and processes, we assume a base-case material utilization efficiency of 50%, meaning that half of the sourced material is contained in the thin films of finished products, and the other half is wasted. We also consider values of 80% in our low energy input case, and 20% in our high energy input case. We assume that the factory product yield is high (approaching 100%) for all cases since business viability requires that defective products be minimal. We do not explicitly consider the energy implications of potential recovery and recycling of the wasted materials, which can be expected for high value materials such as platinum and iridium, but may not be economically viable for lower value materials such as iron and silicon.

Our base-case photocathode material is amorphous silicon, though other potential materials include InP and Cu_2O. Our base-case photoanode material is $BiVO_4$, a moderate bandgap photoanode, though other potential materials include a-Si, WO_3, Fe_2O_3 (hematite), and GaAs. Amorphous silicon is a buried junction device, meaning that, in principle, it can be incorporated to be photoanode or photocathode. If it is integrated with

$BiVO_4$ or Fe_2O_3, one would expect it to be polarized so that its back, non-illuminated side is the HER electrode. If, on the other hand, it is integrated with InP, one would expect it to be polarized such that its back, non-illuminated side acts as the photoanode. Our high energy input case considers GaAs and InGaP photoelectrodes, and our low energy input case uses a-Si and Fe_2O_3 photoelectrodes. We acknowledge that not all combinations of materials we consider would have the required properties for effective PEC cells, *e.g.* sufficient photovoltage to split water, appropriate bandgap combination to achieve specified efficiency, and adequate stability against corrosion. Nevertheless, we consider them as representative examples in terms of embodied energy of a diverse range of materials and fabrication processes.

Potential HER catalyst materials for acidic or basic electrolyte solutions include Pt, NiMo, Co_2P, and Fe_3P. Potential OER catalyst materials for basic solutions include NiO_x, CoO_x, and $NiFeO_x$.[32] For OER under acidic conditions, only IrO_x is currently available and new catalyst discoveries will be necessary to provide alternative materials. Our base-case analysis assumes the use of Pt for HER catalyst and IrO_x for OER catalyst. The same materials are used in our high energy input case. Our low energy input case considers Fe_3P as HER catalyst and $NiFeO_x$ as OER catalyst. We assume a catalyst layer thickness of 1 nm in all cases. This may overestimate the amount of Pt required for HER catalysis, as recent research suggests that much lower Pt loading may be effective.[33]

We assume the use of a TiO_2 protective layer to prevent corrosion of the photoelectrodes.[34,35] In our base case we use a 60 nm thick TiO_2 layer, and we consider 30 nm and 120 nm thick layers in the low and high input cases, respectively. We assume the use of a 50 nm thick TCO layer made of fluorine doped tin oxide (FTO) in our base case, and a 10 nm thick FTO layer in out low energy input case. In our high input case, we consider a 100 nm thick layer of indium tin oxide (ITO) TCO, though this material may not be suitable if temperatures higher than 200 °C are needed in other fabrication processes.

We include the substrate for the thin film assembly as an active material because the electrical charge is transported through it. We consider a substrate of stainless steel, upon which the thin film layers are deposited. We select stainless steel because it is electrically conductive, flexible and resilient enough for use in roll-to-roll processing, and generally chemically resistant to acidic and basic environments. Different types of stainless steel are more resistant to acidic or basic conditions, so an appropriate type must be selected depending on the electrolyte solution. A 0.1 mm thick substrate is used in our base case. We consider a 0.2 mm thick substrate in our high energy input case, and a 0.05 mm thick substrate in our low energy input case.

Membranes of the PEC devices must be impermeable to the produced hydrogen and oxygen, and conductive to cations or anions. The most commonly used cation membrane material is perfluoro-sulfonic acid (PFSA), available commercially as Nafion®.[36] The required thickness of PFSA membrane depends on the device design and is assumed to total 50 μm for our base case. Our high energy input case assumes a 70 μm thick membrane, while our low energy input case uses a 30 μm thick membrane. Based on Zhai *et al.*,[10] the primary energy requirement for supplying raw materials for PFSA membrane production is estimated at 140 MJ per m^2 of membrane. Due to the geometry of the louvered device (Fig. 2), which is established based on computational modelling for optimized ionic transport in electrolyte,[17] the membrane area is equal to 8.8% of the cell area, resulting in an energy use for membrane raw materials of 12 MJ per m^2 of cell area.

We consider the use of 1 M H_2SO_4 solution as electrolyte, though we note that some of the electrode and catalyst materials would not be stable in an acidic environment. Alternatively, an electrolyte such as KOH could be used to create a basic environment. Production of 1 kg of KOH requires over 10 times as much energy as production of 1 kg of H_2SO_4. However, this would have little impact on overall net energy, because 1 M H_2SO_4 electrolyte is responsible for only 0.07% of the total energy use for initial production of the facility. If 1 M KOH were used instead, this amount would increase to 0.7% of total initial energy use.

2.2.2. Embodied energy of inactive module materials. This category includes energy used for extraction, processing, and transportation to the cell factory gate of materials that are not active in the solar energy to fuel conversion process but are nevertheless essential to the performance of the device. These module materials include the transparent front cover, back cover, perimeter frame, and cell support ribs.

A module is 1 m wide and 1.2 m high, and is encapsulated on front and back by 2 mm thick float glass panes. We select glass as the encapsulation material due to its rigidity, transparency (a requirement only for the side facing the sun), resistance to harsh chemical environment, and relatively low embodied energy compared to metals or plastics. Properties of six potential encapsulation materials are detailed in Table S2 of the ESI,† and additional information on glass properties and material selection criteria is in Section S3 of the ESI.† We consider glass thicknesses of 3 mm and 1 mm in a sensitivity analysis. Use of 1 mm glass in the low case may be possible, because the glass is not freestanding but is adhered to periodic ribbed supports that reduce maximum span length and make the entire module a discrete structural element with glass skin and PVC webs.

For configurations that need to operate in basic electrolyte conditions, it will not be possible to use glass in direct contact with the electrolyte because the glass will etch over time. The glass may be protected by a thin polymer coating that is resistant to strong base, such as polyvinyl chloride, polypropylene, or ethylene–propylene diene monomer (EPDM).[37] The embodied energy of a 0.1 mm thick polypropylene layer is about 7 MJ m^{-2}. For comparison, the embodied energy of a 2 mm glass pane is 64 MJ m^{-2}. Covers of polycarbonate and poly(methyl methacrylate) may be used instead of glass, although their embodied energy is significantly higher: respectively about 260 MJ m^{-2} and 340 MJ m^{-2} for 2 mm thickness (see also Table S2, ESI†).

A molded PVC perimeter frame surrounds the module, securing the glass panes and containing the electrolyte solution. We consider 3 alternative designs for the perimeter frame with low, medium (base case), and high material inputs (detailed in ESI,† S4). A molded PVC ribbed framework

supports the membrane and the thin-film substrate, and is adhered to the two glass panes (see Fig. 2). We do not conduct modeling of oxygen gas flows, but assume the generated O_2 is simply vented. This requires further consideration, as a pressure difference between anodic and cathodic chambers may raise structural issues if O_2 is released uncontrolled. To avoid this, valves may be needed to ensure O_2 is released at a rate commensurate with H_2 evolution. There could be advantages to collecting and using the O_2 produced from water splitting, rather than considering it as a waste product to be disposed of. The embodied energy of O_2 collected from a large-scale PEC system was estimated at less than one-fifth that of O_2 derived from conventional separation processes.[11] The O_2 could be used as an input to other low-carbon energy systems, *e.g.* oxy-fuel CO_2 capture technology, thus employing industrial symbiosis to improve overall performance.

Our modeling assumes a generic 10% solar transmittance loss due to absorption, scattering and reflection, but does not specifically consider refection from the glass surface. An anti-reflective (AR) coating may be applied to the surface of the glass cover, to reduce reflection loss that may be significant. A typical AR coating is MgF_2, which is often deposited using vacuum evaporation methods. As discussed below, such thin film deposition processes may be energy intensive, thus the energy inputs for applying an AR coating should be weighed against the increased capture of solar energy. As an illustrative example, if we assume that an AR coating reduces reflective losses by 4%, this corresponds to about 340 MJ of increased hydrogen produced by a m^2 of cell during a 10-year life span with 10% STH efficiency. As this is roughly the same magnitude as the energy needed for thin film deposition (see Section 2.2.3), the net energy benefit of a conventional AR coating is questionable, and is not considered further. Reducing the energy intensity of thin film deposition processes, as discussed in the next section, may make AR coatings more favorable.

2.2.3. Energy intensity of active cell material fabrication. This category includes energy use for thin-film deposition of active cell materials, as well as for membrane fabrication. Data for manufacturing of thin film photovoltaics offer the most relevant information since the processes used are expected to be applicable to solar fuels technologies, although the materials sets are somewhat different. A variety of thin film deposition techniques are available, including physical vapor deposition (PVD) methods[38] such as evaporation, sputtering, laser ablation, and arc-based emission; chemical vapor deposition (CVD) methods[39] such as thermal, plasma enhanced CVD, combustion CVD, and atomic layer deposition; and solution-based methods[40,41] such as spin-coating, inkjet printing, spray pyrolysis, and gravure printing. These thin film deposition techniques may use energy for various purposes, *e.g.* vacuum, ion generation, heating, and cooling, which result in a wide range of process energy intensities.[42] Process energy use may vary depending on pressure (high vacuum *vs.* low vacuum *vs.* atmospheric pressure) and required pumping speed, temperature (1000 °C range *vs.* 100 °C range *vs.* room temperature), film thickness (which directly correlates with processing time), precursor or source material (gas *vs.* solid), and other parameters. Economies of scale are seen in deposition energy use, with larger facilities using much less energy per square meter of deposited area.[43] This places constraints on how useful energy intensity data can be acquired for various processes. For example, theoretical values of energy use for vacuum pumping can be calculated for a single evacuation event. At industrial scale, however, load locks and transfer chambers are used instead of repeated venting-evacuation cycles, and efficiencies are gained by use of differential vacuum pumping of relatively small volumes for short times.[44] The geographic location of a manufacturing plant may also affect the energy intensities of production.[45]

In our base case we assume the use of a state-of-the-art integrated inline coater, where multiple layers are deposited sequentially in the same vacuum chamber, thus minimizing the total energy use for vacuum pumping. Reviews of LCA studies of thin-film PV technologies[30,46] show that direct process energy for thin-film deposition (of *e.g.* a-Si and CdTe PV modules) ranges from a low of 130 MJ m^{-2} to a high of 1150 MJ m^{-2}, with most examples being in the range of 300–500 MJ m^{-2}. Although the use of PV manufacturing as a model for photoelectrochemical device fabrication does not fully capture likely processes, it is valuable for providing an initial process energy estimate. We select 400 MJ m^{-2} as our base-case value for thin-film deposition energy, representing current best practice in an integrated inline deposition process. As a higher energy input case, we select 800 MJ m^{-2} representing current average practice, which may involve non-integrated processes using separate sequential deposition lines. As a lower energy case, we consider a room temperature, atmospheric pressure, solution-based deposition method. A recent LCA of solution-processed perovskite solar modules[47] shows primary energy use for thin-film fabrication as low as 60 MJ m^{-2}, which we adopt as our low energy input case. Our low input case considers the use of amorphous Si electrodes made with a solution phase process, which is currently at an early stage of development and has not been deployed into manufacturing.[48] As currently practiced, it requires strictly water and air-free chemical handling and process conditions that will increase the complexity and energy intensity of the method. We consider nevertheless the scenario, to determine the bounds of potential system benefits from technological improvements.

Energy is used for both material supply and fabrication of the membrane; material supply was discussed in Section 2.2.1. Based on Zhai *et al.*,[10] the primary energy requirement for fabrication of PFSA membrane is estimated to be 166 MJ per m^2 of membrane. Due to the geometry of the louvered device (Fig. 2) the membrane area is equal to 8.8% of the cell area, resulting in an energy use for membrane raw materials of 15 MJ per m^2 of cell area.

2.2.4. Energy intensity of module assembly. This category includes encapsulation steps (*e.g.* cutting, pressing), other ancillary supplies (*e.g.* miscellaneous process chemicals), and indirect industrial processes (*e.g.* environmental control of manufacturing facilities such as space heating, cooling, ventilation, and air filtration). Based on Zhai *et al.*,[10] we assume a base-case value for module assembly of 241 MJ per m^2 of cell area.

This parameter is subject to considerable uncertainty, and literature on energy use for large-scale PEC cell assembly is absent. We therefore assume a broad range of values in a sensitivity analysis, varying this parameter between 50% and 200% of base-case value.

2.3 Balance-of-system (BOS)

The net energy balance of PEC H_2 production is determined not only by the cell and module components such as photoelectrodes, catalysts, and encapsulation, but also by the BOS requirements such as structural supports, manifolds and pipes, pumps, compressors, storage tanks, pipelines, roads and monitoring systems. The modelled BOS characteristics are briefly described below, and elaborated in more detail by Sathre *et al.*[11] As discussed above, the modeled 1 GW hydrogen production facility is configured on five hierarchical levels: cells, modules, panels, fields, and facility. The two smallest levels, the cell and module, were described above in Section 2.2. The remaining three levels comprise the BOS (Fig. 3). A total of 24 individual modules are mounted onto a truck-transportable "panel" of ~29 m^2. A "field" contains 1000 panels in a fixed flat array format, plus gas compression and storage, occupying 120 000 m^2. Finally, the 1 GW (annual average) "facility" comprises 1600 fields occupying 190 km^2 in the base-case of 10% STH efficiency.

A "panel" is 12.0 m long by 2.4 m wide, and includes a structural frame upon which 24 PEC modules are mounted. Panels include onboard monitoring and diagnostics sensors, and pipe manifolds for transferring fluids to and from each module. Panels and modules have standardized fluid and data connections so they can be installed and removed from the facility relatively easily to facilitate maintenance. The total weight of a complete panel is about 510 kg without electrolyte and 690 kg including electrolyte. The panels are fixed and are tilted towards the equator at an angle equal to the local latitude, here assumed to be 34°.

In the present study, our panel-level modeling differs in two ways from our previous work.[11] First, we have redesigned the panel structural elements to reduce the amount of steel required. The new design accommodates a lighter load (due mainly to thinner modules containing less electrolyte), and has a slightly more complex profile using two steel sections welded together rather than a single larger steel section. This reduces the amount of steel in each panel by 39%, from 340 kg to 207 kg. The panel structural design is described in Section S5 of the ESI.† The second change in panel design is that the inactive area (percent of gross panel area that is not active solar collection area) is increased to 10%, from the 5% that we assumed in our previous analysis. This change is due to the supporting ribs in the louvered PEC modules (see Fig. 2) that occupy surface area but do not capture solar energy, which were not present in the earlier microwire cell design. The active area is now 25.8 m^2 per panel. This change increases the number of panels needed to produce 1 GW of hydrogen, compared to the number calculated by Sathre *et al.*[11]

A "field" comprises 1000 panels plus compression and storage infrastructure for one day's production of H_2. Spacing between panels is assumed to be 0.5 m end-to-end. Spacing between rows of panels is 9.5 m, based on a 10° shading angle. While the choice of size for a field is somewhat arbitrary, it represents an important organizational principle, that of distributed water supply, gas collection and compression, at a level intermediate between panel and facility levels, with all panels located within 50 m of an access road for replacement with a mobile crane. In a final, optimized engineering design, there might be multiple levels of intermediate organization in a facility of this size, and the unit size could be considerably larger or smaller than the 1000 panels envisioned here. The field level is also envisioned to be of standardized spatial dimensions and therefore completely modular; an area of land

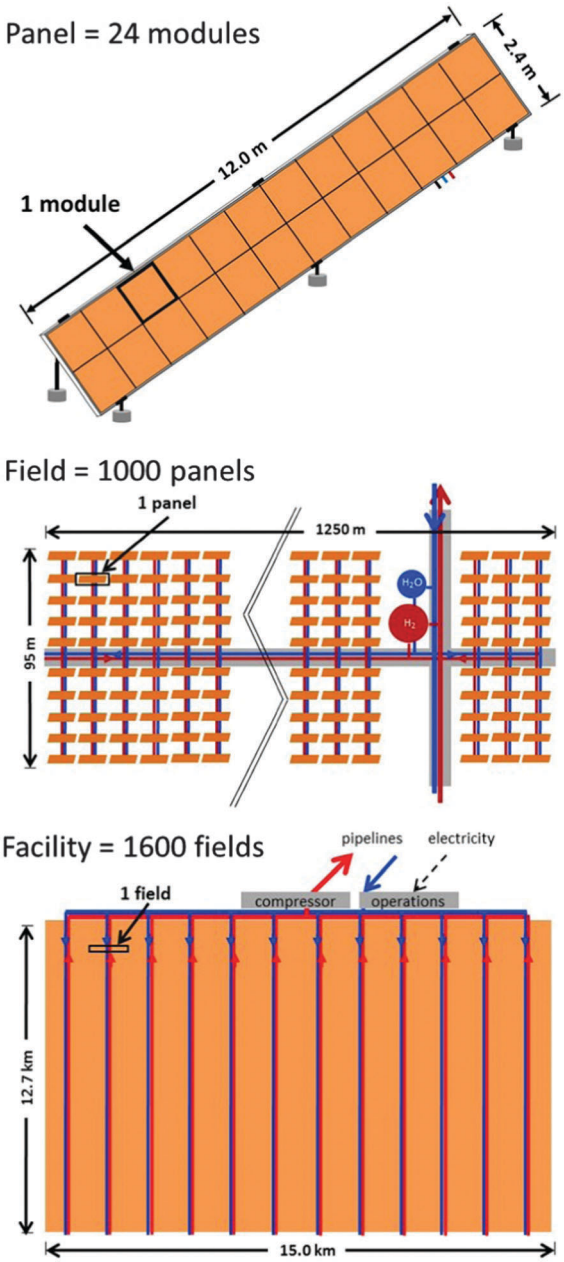

Fig. 3 Three hierarchical levels (panel, field and facility) comprise the BOS of the 1 GW (continuous annual average) hydrogen production facility.

at the facility level may have a complex topography and not occupy a simple rectangular area, but at the level of a field the installation could be completely regular and uniform.[5]

The entire "facility" aggregates production from 1600 fields, with a 90% capacity factor (*i.e.* on an average day 90% of the panels are producing H_2). Under base-case 10% STH efficiency, a total of 41.1 km^2 of active PEC solar collection area is needed, occupying 190 km^2 of land area. The facility is assumed to be located in the southwest US in an area of high insolation. Solar resource data are taken from NREL,[49] and are the average of monthly mean flat-panel insolation at four sites: Phoenix, Daggett, Tucson, and Las Vegas. The annual average solar insolation is 276 W m^{-2}. In a sensitivity analysis, we also consider insolation data from a more representative selection of US sites: Charlotte, Omaha, Salt Lake City and Chicago. Details on solar insolation at each site are in Section S6 of the ESI.† We assume a life-span of 40 years for the facility. At the end of its service life, the facility will require decommissioning. This entails removing or remediating the infrastructure and equipment comprising the facility, and its safe disposal or recycling. Following the method used in the series of energy system life cycle assessments summarized by NETL,[50] we assume that decommissioning requires 10% of the energy used for initial construction of the facility (here we consider only the energy used for BOS construction, because end-of-life management of cells and modules are discussed elsewhere). While in this study we analyze a large-scale 1 GW facility, an interesting topic for future research is the suitability of smaller modular PEC facilities for deployment in the manner that PV is installed at smaller and variable scales.[51]

To determine the high input and low energy input values of the two BOS characteristics (Table 1), we conducted Monte Carlo simulations to estimate uncertainty introduced by interactions between multiple individual parameters describing the BOS. Simulation was conducted using Oracle® Crystal Ball software. Triangular probability distributions were assumed for each parameter based on low, base-case and high values (Table S3, ESI†). Based on the outcome distribution of 10 000 simulations with simultaneous variation of each variable, the mean values of initial and ongoing BOS energy inputs are used as base-case parameter values, and 90% confidence intervals are used as high input and low input parameter values. Because the BOS requirements of a fixed-output facility will depend on STH efficiency and cell life span, we conducted nine separate simulations considering each combination of these parameters. Outcomes of the Monte Carlo simulations are shown in Fig. S7 of the ESI.†

3. Results and discussion

Table 2 shows the energy inputs for materials and fabrication of the cells and modules. In our base case, a total of 981 MJ primary energy will be needed to produce modules with 1 m^2 of active cell area. This energy input rises to 1843 MJ in our high input case, and drops to 373 MJ in our low input case. Fabrication of active cell components is the largest single energy input in the base case, mainly due to thin film deposition process energy. Energy use for both materials and fabrication of inactive module components are the next biggest inputs. Energy use for supplying active cell materials is the least significant input. There is a tenfold range in energy use for active cell fabrication, from ~70 MJ m^{-2} in the low energy input case, to over 800 MJ m^{-2} in the high energy case. Progress in reducing the energy intensity of thin film deposition processes is an opportunity to improve net energy performance.

Table 2 Summary of high input, base case, and low input values of energy use for PEC cell and module production (MJ primary energy per m^2 active cell area)

	High energy input	Base case	Low energy input
Active cell materials	194.3	93.3	40.6
Thin-film materials	53.9	18.1	0.8
Membrane materials	15.6	12.2	7.6
Conductive substrate	123.4	61.7	30.9
Electrolyte	1.4	1.4	1.4
Inactive module materials	348.5	231.8	143.0
Glass window[a]	106.2	70.8	35.4
Glass back cover[a]	106.2	70.8	35.4
Supporting ribs	51.5	51.5	51.5
Perimeter frame	84.7	38.7	20.8
Active cell fabrication	818.6	414.5	69.1
Thin-film deposition	800.0	400.0	60.0
Membrane fabrication	18.6	14.5	9.1
Inactive module fabrication	481.9	240.9	120.5
Total without BOS	1843	981	373

[a] The embodied energy values for glass shown here are greater than those discussed in Section 2.2.2 and listed in Table S2 (ESI), because these values are expressed per m^2 of active cell area. Active cell area is 90% of total module area.

We observe that several of the materials considered here as raw materials for cell or module production (*e.g.* stainless steel, glass, PVC) are all the finished products of earlier production processes, each of which required their own raw materials. Thus, the energy use breakdown begun in Table 2 could further distinguish the embodied energy of these materials, *e.g.* energy used for mineral extraction, ore processing, transport, and refining. For example, a typical soda-lime glass composition used for window glass consists of ~60% silica sand, ~20% sodium monoxide derived from soda ash (sodium carbonate), and ~18% calcium monoxide derived from limestone (calcium carbonate).[52] The raw materials (sand, limestone and soda ash) are combined and heated, typically using methane fuel. The melted glass is formed into sheets on a float bed, and cooled until solid. The glass sheets are then cut to size and annealed. Heating the raw materials to melting temperature is the most energy-intensive process step in glass production in continuous furnaces, contributing over half of the embodied energy of the finished product. Supply of raw materials (silica sand, limestone, soda ash) including extraction, primary processing and transport, contributes less than 15% of the embodied energy (authors' calculation based on ref. 52 and 53). Another example

is stainless steel production. There are numerous grades of stainless steel that are produced, the most common being 18-8 type comprised of 74% Fe, 18% Cr and 8% Ni. Each of these metals is obtained from ores of various composition. Energy use for mining, beneficiating and transporting the metal ores contributes only about 8% of the total embodied energy of stainless steel.[54] Most of the embodied energy is due to high temperature thermochemical refining processes.

A breakdown of the embodied energy of the precursor materials used for thin film layers is shown in Table 3. The variations between the high energy input case, base case, and low energy input case are due to different selection of materials, different layer thicknesses, and different values for the material utilization efficiency and the ratio of embodied energy of the refined element to that of the precursor materials. The totals in Table 3 are included in Table 2 under the heading "Thin film materials". Details on these materials and various other materials used in thin films are in Section S1 of the ESI.† Comparison to Table 2 shows that energy use for supplying active cell materials is a minor part of total life cycle energy use.

Fig. 4 compares the production energy use of the louvered thin-film cell design analyzed here to the silicon microwire cell design studied by Zhai *et al.*[10] The louvered thin-film cell design uses substantially less energy for production (base-case value of 981 MJ m^{-2}) than the silicon microwire design (base-case value of 2110 MJ m^{-2}). Major improvements are due to reduced energy for fabricating photoactive components, and reduced embodied energy of inactive materials. This demonstrates that innovative cell design and manufacture can improve net energy performance.

Fig. 5 shows the energy inputs for initial BOS production and for ongoing BOS operation and EOL, under different STH efficiencies and with low, base and high energy inputs. These BOS energy use values are based on the Monte Carlo simulation results detailed in Section S7 of the ESI,† and are normalized to annual energy use. The ongoing energy inputs, mainly for BOS operation but also including EOL, are found to be substantially greater than the initial energy inputs for BOS production.

Fig. 6 shows the annual energy balance of the H_2 production facility in operation, under base-case conditions at 10% STH efficiency. The energy content of the H_2 produced corresponds to 31.5 PJ of primary energy per year, which is equivalent to 1 GW continuous power for one year. From this positive value is subtracted the primary energy needed to operate the production system. The largest single energy use is for gas compression,

Table 3 Embodied energy of precursor materials to the thin film layers, for the high input, base case, and low input cases (MJ primary energy per m^2 active cell area)

Thin film layer	High energy input	Base case	Low energy input
OER catalyst	5.8	2.9	0.001
Protective layer	2.4	0.60	0.15
Photoanode	8.2	1.1	0.56
TCO	5.5	0.17	0.02
Photocathode	9.5	2.0	0.02
HER catalyst	22.6	11.3	<0.001
Total	53.9	18.1	0.75

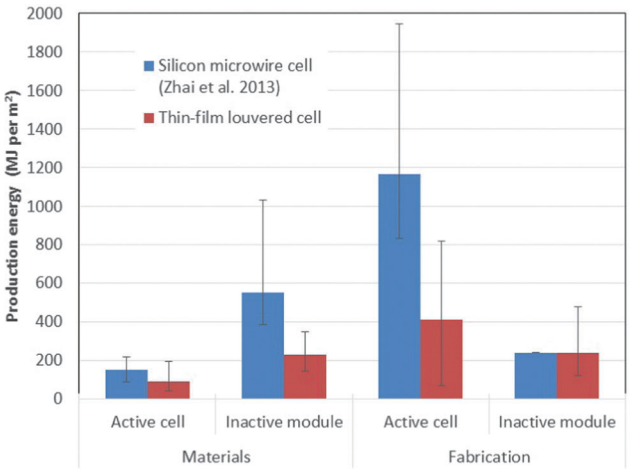

Fig. 4 Production energy use for louvered thin-film cell design is substantially lower than that estimated by Zhai *et al.*[10] for a silicon microwire cell design.

which uses 5.0 PJ of primary energy per year. It may be possible to reduce this compression energy need by designing cells to produce H_2 at higher pressure, using an overpotential of 0.06 eV per atm to drive H_2 production at elevated pressure.[55] Maintaining cells and modules above atmospheric pressure would entail trade-offs between the decreased energy requirements for gas compression and the higher performance needs of other components including module encapsulation and pipes. Module replacement is the second largest energy input, using 4.1 PJ per year under steady-state conditions with a 10-year cell life span (*i.e.* 10% of all modules in the facility are replaced each year). Module replacement includes full material and fabrication energy for new cells and modules; material recycling is not explicitly considered. The energy for module replacement is less than half of the 8.7 PJ per year estimated in our previous work,[11] due to the lower energy intensity of cell fabrication and the reduced module material use (Fig. 4). Energy use for module replacement depends strongly on cell life span; error bars in Fig. 6 show that 8.3 PJ per year is needed with a 5-year life span, and only 2.1 PJ per year is used with a 20-year cell life span. Module heating to avoid electrolyte freezing on cold winter nights was estimated in our previous work to require 1.5 PJ per year.[11] The internal convection coefficients of the louvered design are different from the previous microwire system, resultant from the changes to the internal cell geometry, but we assume this will not significantly change the heating energy requirement. The need for module heating is discussed further in Section S8 of the ESI.† Energy use for gas handling, water supply and facility operations is minor. In total, about 11.4 PJ of energy inputs are needed per year, resulting in a net energy delivery of 20.1 PJ of primary energy per year, under base-case conditions. In Fig. 6, error bars for Module heating represent the coldest and warmest of four modeled locations, and for gas compression, gas handling, water supply and facility operation are based on parameter sensitivity modeling. The error bars for net energy delivered are the sums of the other error bars.

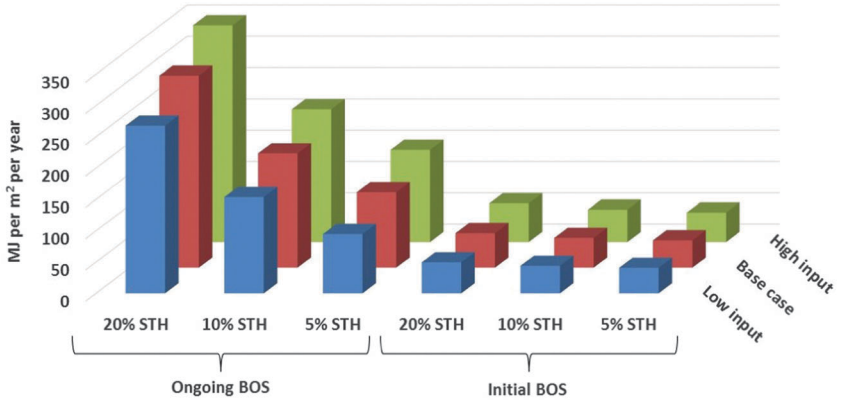

Fig. 5 Energy use for initial and ongoing BOS, under different conditions of STH efficiency and with high input, base case, and low input parameter values (MJ primary energy per m^2 active cell area per year).

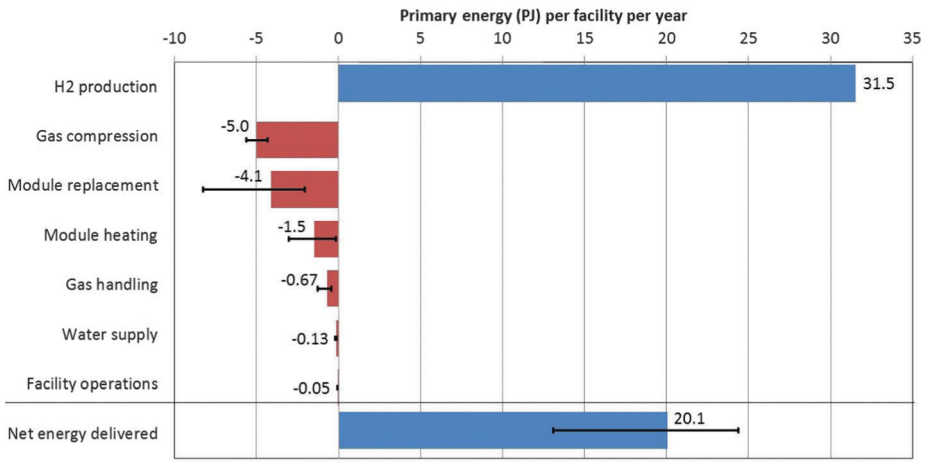

Fig. 6 Annual energy balance (PJ $year^{-1}$) of 1 GW (annual average) H_2 production facility in operation under base-case conditions.

Fig. 7 shows the one-time energy inputs required to produce and decommission the 1 GW H_2 facility. Under base-case conditions, initial construction will need a total of 72.9 PJ of primary energy. The energy use for materials and fabrication of cells and modules represents the energy investment to initially equip the complete facility with PEC cells and modules; thereafter, energy use for periodic replacement of the cells and modules is accounted for in the annual energy balance (Fig. 6). The estimated energy input for decommissioning of the facility at the end of its service life is 3.4 PJ. These one-time inputs are compared to the annual delivered net energy of the facility in operation (from Fig. 6), shown as a dashed line. Under base case conditions, it will take about 4.1 years of operation to deliver energy that is equivalent to that used for initial construction and final decommissioning. Over the 40-year projected service life of the facility, the EROEI is 2.34 and the life cycle primary energy balance is +720 PJ. This net energy performance is substantially better than that estimated in our previous analysis of silicon microwire cell design.[11] The current energy payback time is half of the 8.1 years estimated previously, the EROEI is 29% higher than the previous estimate of 1.66, and the current energy balance is 31% higher than the +500 PJ estimated by Sathre *et al.*[11] The improved net energy performance is largely due to the reduced energy inputs for cell and module production, which results in lower initial energy use for facility construction (Fig. 7), as well as lower ongoing energy use for cell replacement (Fig. 6).

Fig. 8 shows the change in the three net energy metrics (life cycle energy balance, EROEI, energy payback time) due to one-at-a-time variation of eight individual parameters between their low and high values. Two of the parameters describe the embodied energy of cell and module materials, two describe the energy intensity of cell and module fabrication processes, two describe the initial and ongoing energy use of the BOS, and two parameters describe cell performance (STH efficiency and cell life span). STH efficiency is overwhelmingly the parameter variation causing the most significant change in all three metrics. Current prototype cells typically range from 5% to 10% STH efficiency, with 20% being an aspirational upper limit. Variation of PEC cell life span is the second most significant parameter. The range of energy use for active cell fabrication, dominated by thin-film deposition energy use, is the third most significant parameter. Variation in ongoing energy use for BOS operation is the next most significant. The modeled range of variation is much less significant for other parameters,

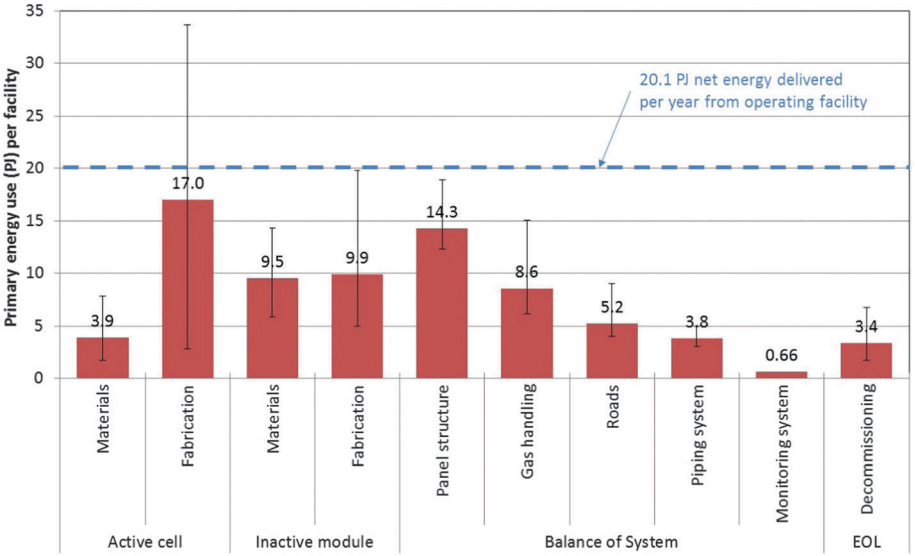

Fig. 7 One-time primary energy inputs (PJ) required to construct and decommission a 1 GW (annual average) facility. For comparison, the base-case annual delivered net energy of the completed facility in operation is shown as a blue dashed line.

including inactive module materials and fabrication, active cell materials, and initial BOS energy use. We also observe the importance of solar insolation levels, which are a function of location. Using insolation data from north-central US locations instead of the base-case southwest US locations, the EROEI is reduced from 2.34 to 1.74, and the energy payback time is increased from 4.1 years to 6.8 years (not shown in Fig. 8).

We examined the question of whether more efficient and longer lived devices that require higher energy inputs for materials or fabrication will exhibit improved net energy performance, compared to less efficient and shorter lived devices with lower energy input. To explore these relations, we compare three PEC systems, with all six characteristics (from Table 2) at the low input, base case, and high input values, respectively. Furthermore, we assume that the system with low inputs performs at 5% STH efficiency and 5-year life span, the base case system performs at 10% STH efficiency and 10-year life span, and the high input system performs at 20% STH efficiency and 20-year life span. We emphasize that such quantitative relations are purely illustrative, and are based neither on laboratory experience nor theoretical computation. Nevertheless, given the plausible ranges we consider of energy inputs, STH efficiency and life span, such exploratory analysis can provide insight into broad trends and sensitivities. Fig. 9 shows that under the modeled conditions, the high input system gives much better overall energy performance. The low input system, despite lower energy inputs than the other systems, delivers reduced life cycle net energy due to its lower hydrogen production rate and shorter life span. This suggests that high STH efficiency and long life spans are primary design requirements for PEC systems, even if such performance requires additional energy and material inputs for production and operation.

Our model already assumes re-use of panel support structure, manifold pipes, and sensors upon replacement of PEC modules. If inactive module materials (glass window, glass back cover, PVC support ribs and PVC frame) are also re-used at the end of cell life span, the system performance improves because less energy is required to produce replacement cell materials. The energy balance increases by 5% to +760 PJ, the energy return on energy invested increases 8% to 2.5, and the energy pay-back time decreases by 5% to 3.9 years. The suitability of re-use of glass encapsulation materials may be limited by the possible damage to the glass after years of use, *e.g.* by etching by wind-blown sand. While there are clear energy benefits of direct re-use of glass products (*e.g.* glass containers), the energy benefits are much less if the recovered glass must be melted and reconfigured.[53]

We also conduct a scale-up analysis to estimate required quantities of thin film materials and identify potential constraints in material availability. We consider three hydrogen demand scale-up scenarios of varying extent, which are detailed in Section S9 of the ESI.† The lowest demand scenario assumes that 10% of US light-duty vehicle demand in 2040 would be satisfied by hydrogen from our modeled facilities. This amount of scale-up is expected to require 14 facilities producing 1 GW (continuous annual average) each. The middle scenario assumes 100% of US light-duty vehicle demand in 2040 would be satisfied by facility-generated hydrogen, and would require 142 facilities of 1 GW each. The highest demand scenario assumes that 100% of global light-duty vehicle demand in 2040 would be satisfied by facility-generated hydrogen, and is projected to require 850 facilities of 1 GW each. We calculate the amount of thin film materials that would be required annually for these hydrogen production facilities, assuming an STH efficiency of 10%, a cell life span of 10 years, and a material utilization efficiency of 50%. We compare the annual scenario requirement for each element to the 2014 global primary mine production of each element,[56] as an initial estimate of scale-up feasibility.

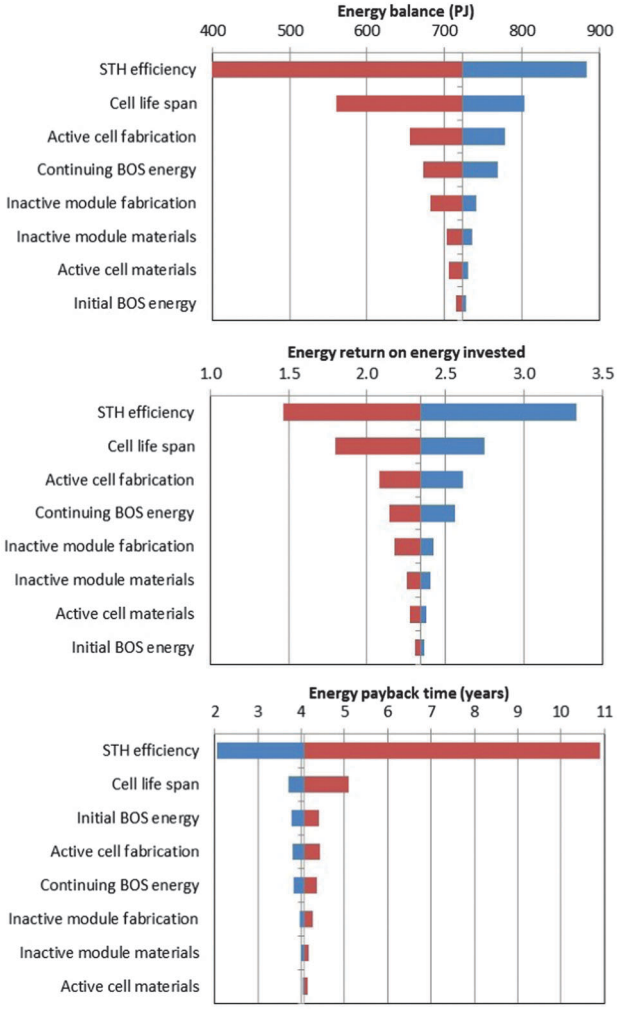

Fig. 8 Effect on system performance metrics of individual variation of key parameters from their base-case values. Top image shows energy balance; middle image shows EROEI; bottom image shows energy payback time. Blue bars indicate improved net energy performance compared to base-case, while red bars indicate reduced net energy performance.

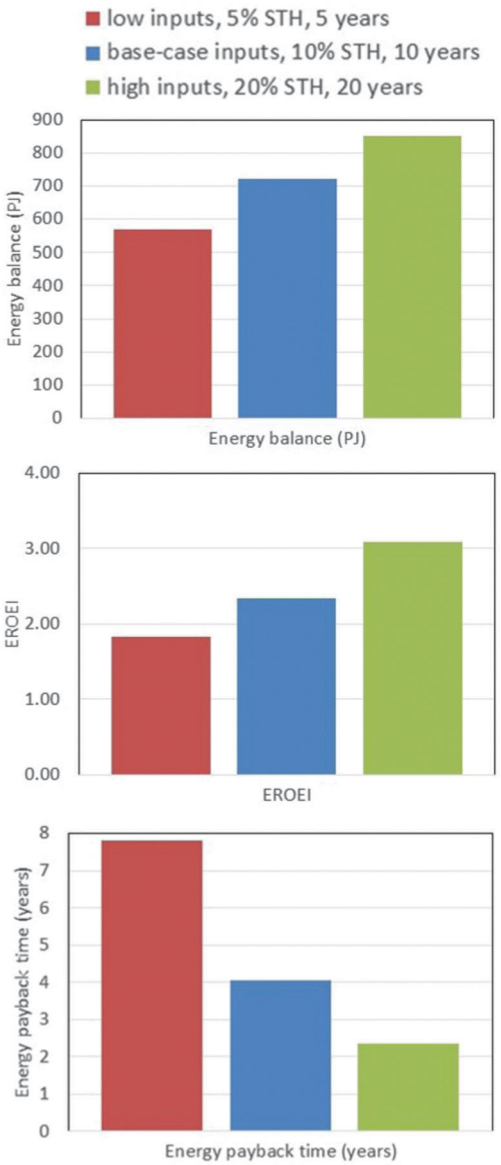

Fig. 9 System performance metrics of 3 combinations of parameters: low input and low performance (left bars), base case inputs and base case performance (middle bars), and high input and high performance (right bars).

For many of the thin film materials, particularly the abundant materials such as Si, Fe, Ni, Cu, P, Sn, Ti and V, large-scale deployment of PEC hydrogen generation would require a very low proportion of current global mine production, suggesting that supply constraints are unlikely. At the lowest scale-up level (10% of US demand by 2040), only tellurium (as part of CdTe photoelectrode) and iridium (as OER catalyst) show likely supply constraints, each requiring over 30% of current production rates of the elements. If scaled-up to meet 100% of US demand by 2040, gallium (as part of GaAs or InGaP photoelectrodes) and indium (a component of InP and InGaP photoelectrodes as well as ITO TCO layers) begin to show likely supply constraints. At the 2040 global scale-up level, platinum (as HER catalyst) and bismuth (as part of $BiVO_4$ photoelectrode) supply would likely be constrained, and the quantities of Te, Ir, In and Ga required annually would exceed current primary production rates of these elements. We note, however, that we may significantly overestimate the amount of Pt needed for HER catalysis, as indicated by recent research.[33] Results of the scale-up material use analysis are detailed in Section S9 of the ESI.† An important caveat when comparing against current mine production is that future production may differ substantially due to changes in economic demand or extraction and processing technology. Resource constraints for key materials may be encountered due to limited absolute quantities of materials, or to conflicts with other potential uses of the materials. Some industrially important elements such as In, Bi, Co, Ga and Cd are extracted as by-products of other mining processes, thus have low price-elasticity of supply.[57] Potential material constraints are yet to be fully incorporated into most technology assessments. The LCA framework traditionally includes a "resource depletion" impact category, though the longer time scale and non-linear

response of that impact compared to some other categories makes objective comparison difficult. The emerging metric of "material criticality" takes into account two aspects: the risks to reliable supply of a material, and vulnerability of a technological system to a potential supply disruption of the material.[58]

4. Conclusions

We have used prospective life cycle assessment, an approach to provide early insight on emerging technologies, to understand the potential net energy implications of eventual large-scale manufacturing, deployment, and operation of a PEC hydrogen production system. We measured three indices of net energy performance (life cycle primary energy balance, energy return on energy invested, and energy payback time), as indicators of system-wide energetic viability of the technology.

This prospective LCA has identified several priorities for PEC development efforts. First, the STH conversion efficiency of cells has a very strong impact on net energy viability of a PEC H_2 system. STH efficiency remains a primary system requirement. Our modeling suggests that STH efficiency well above 5% is needed for net energy viability. Second, the cell life span also has strong net energy significance; a cell with life span less than five years will be energetically challenged. The third most important parameter is the energy intensity of cell fabrication, where low-energy thin film deposition processes will improve performance. The other system characteristics are less important, including inactive module fabrication, active cell materials, inactive module materials, and BOS energy use. Facility location is important, and high-insolation sites should be selected for improved net energy. STH efficiency and cell life span remain the predominant source of system-wide variability and uncertainty regarding PEC net energy performance. This suggests that a marginal increase in energy use for cell production will be energetically rewarded to the extent it increases STH efficiency or cell life span.

This work has demonstrated that innovative design and manufacture can improve the net energy performance of PEC systems, and could be expanded to include concentrating PEC devices (*e.g.* ref. 59). Concentration may improve net energy performance because of the potentially higher STH efficiency and the use of a smaller active collection area, as has been suggested in an analysis of a PV–electrolyzer system for H_2 generation.[60] However, concentration mechanisms require more inactive materials, *e.g.* for tracking and optics. A detailed net energy analysis could elucidate these trade-offs. The analytical framework could be further improved by quantitatively linking cell production energy with cell performance. Increasing availability of material characterization data[61] should allow robust performance-based analysis of a wide range of potential configurations.[62]

Acknowledgements

This material is based upon work performed by the Joint Center for Artificial Photosynthesis, a DOE Energy Innovation Hub, supported through the Office of Science of the US Department of Energy under Award Number DE-SC0004993.

References

1 S. Chu and A. Majumdar, Opportunities and challenges for a sustainable energy future, *Nature*, 2012, **488**, 294–303.
2 International Energy Agency (IEA), Key World Energy Statistics, Paris, 2014.
3 Intergovernmental Panel on Climate Change (IPCC), Climate Change 2013: The Physical Science Basis, Working Group I Contribution to the Fifth IPCC Assessment Report, 2013. Web-accessed at https://www.ipcc.ch/report/ar5/wg1/.
4 National Academy of Sciences (NAS), Hidden Costs of Energy: Unpriced Consequences of Energy Production and Use, Washington DC, 2010. Web-accessed at http://www.nap.edu/catalog.php?record_id=12794.
5 S. Ong, C. Campbell, P. Denholm, R. Margolis and G. Heath, *Land-Use Requirements for Solar Power Plants in the United States*, National Renewable Energy Laboratory, Report NREL/TP-6A20-56290, 2013.
6 N. Espinosa, M. Hosel, D. Angmo and F. C. Krebs, Solar cells with one-day energy payback for the factories of the future, *Energy Environ. Sci.*, 2012, **5**, 5117–5132.
7 Z. B. Chen, T. F. Jaramillo, T. G. Deutsch, A. Kleiman-Shwarsctein, A. J. Forman, N. Gaillard, R. Garland, K. Takanabe, C. Heske, M. Sunkara, E. W. McFarland, K. Domen, E. L. Miller, J. A. Turner and H. N. Dinh, Accelerating materials development for photoelectrochemical hydrogen production: Standards for methods, definitions, and reporting protocols, *J. Mater. Res.*, 2010, **25**, 3–16.
8 J. Rongé, T. Bosserez, D. Martel, C. Nervi, L. Boarino, F. Taulelle, G. Decher, S. Bordiga and J. A. Martens, Monolithic cells for solar fuels, *Chem. Soc. Rev.*, 2014, **43**, 7963–7981.
9 J. W. Ager III, M. Shaner, K. Walczak, I. D. Sharp and S. Ardo, Experimental demonstrations of spontaneous, solar-driven photoelectrochemical water splitting, *Energy Environ. Sci.*, 2015, **8**, 2811–2824.
10 P. Zhai, S. Haussener, J. Ager, R. Sathre, K. Walczak, J. Greenblatt and T. McKone, Net primary energy balance of a solar-driven photo-electrochemical water-splitting device, *Energy Environ. Sci.*, 2013, **6**, 2380–2389.
11 R. Sathre, C. D. Scown, W. R. Morrow, J. C. Stevens, I. D. Sharp, J. W. Ager, K. Walczak, F. A. Houle and J. B. Greenblatt, Life-cycle net energy assessment of large-scale hydrogen production *via* photoelectrochemical water splitting, *Energy Environ. Sci.*, 2014, **7**, 3264–3278.
12 B. A. Pinaud, J. D. Benck, L. C. Seitz, A. J. Forman, Z. Chen, T. G. Deutsch, B. D. James, K. N. Baum, G. N. Baum, S. Ardo, H. Wang, E. Miller and T. F. Jaramillo, Technical and economic feasibility of centralized facilities for solar hydrogen production *via* photocatalysis and photoelectrochemistry, *Energy Environ. Sci.*, 2013, **6**, 1983.

13 A. C. Nielander, M. R. Shaner, K. M. Papadantonakis, S. A. Francis and N. S. Lewis, A taxonomy for solar fuels generators, *Energy Environ. Sci.*, 2015, **8**, 16–25.

14 G. Peharz, F. Dimroth and U. Wittstadt, Solar hydrogen production by water splitting with a conversion efficiency of 18%, *Int. J. Hydrogen Energy*, 2007, **32**, 3248–3252.

15 A. Fujishima and K. Honda, Electrochemical Photolysis of Water at a Semiconductor Electrode, *Nature*, 1972, **238**, 37–38.

16 S. Y. Reece, J. A. Hamel, K. Sung, T. D. Jarvi, A. J. Esswein, J. J. H. Pijpers and D. G. Nocera, Wireless solar water splitting using silicon-based semiconductors and earth-abundant catalysts, *Science*, 2011, **334**, 645–648.

17 K. Walczak, Y. Chen, C. Karp, J. W. Beeman, M. Shaner, J. Spurgeon, I. D. Sharp, X. Amashukeli, W. West, J. Jin, N. Lewis and C. Xiang, Modeling, simulation, and fabrication of a fully integrated, acid-stable, scalable solar-driven water-splitting system, *ChemSusChem*, 2015, **8**, 544–551.

18 M. R. Shaner, J. R. McKone, H. B. Gray and N. S. Lewis, Functional integration of Ni–Mo electrocatalysts with Si microwire array photocathodes to simultaneously achieve high fill factors and light-limited photocurrent densities for solar-driven hydrogen evolution, *Energy Environ. Sci.*, 2015, **8**, 2977–2984.

19 C. Xiang, Y. Chen and N. S. Lewis, Modeling an integrated photoelectrolysis system sustained by water vapor, *Energy Environ. Sci.*, 2013, **6**, 3713–3721.

20 M. Modestino, M. Dumortier, S. Hashemi, S. Haussener, C. Moser and D. Psaltis, Vapor-fed microfluidic hydrogen generator, *Lab Chip*, 2015, **15**, 2287–2296.

21 M. R. Singh, E. L. Clark and A. T. Bell, Effects of electrolyte, catalyst, and membrane composition and operating conditions on the performance of solar-driven electrochemical reduction of carbon dioxide, *Phys. Chem. Chem. Phys.*, 2015, **17**, 18924.

22 M. Schreier, L. Curvat, F. Giordano, L. Steier, A. Abate, S. M. Zakeeruddin, J. Luo, M. T. Mayer and M. Grätzel, Efficient photosynthesis of carbon monoxide from CO_2 using perovskite photovoltaics, *Nat. Commun.*, 2015, **6**, 7326.

23 T. Arai, S. Sato and T. Morikawa, A monolithic device for CO_2 photoreduction to generate liquid organic substances in a single-compartment reactor, *Energy Environ. Sci.*, 2015, **8**, 1998–2002.

24 Ecoinvent, Ecoinvent v2.2 Life Cycle Inventory (LCI) database, 2012. Web-accessed at www.ecoinvent.org.

25 P. Nuss and M. J. Eckelman, Life cycle assessment of metals: A scientific synthesis, *PLoS One*, 2014, **9**, e101298.

26 E. Williams, N. Krishnan and S. Boyd, Ultrapurity and energy use: Case study of semiconductor manufacturing, Chapter 7, in *Thermodynamics and the Destruction of Resources*, ed. B. R. Bakshi, T. G. Gutowski and D. P. Sekulic, Cambridge University Press, 2014.

27 H.-J. Althaus, M. Chudacoff, R. Hischier, N. Jungbluth, M. Osses and A. Primas, *Life Cycle Inventories of Chemicals*, Final report ecoinvent data v2.0 No. 8. Swiss Centre for Life Cycle Inventories, Dübendorf, Switzerland, 2007.

28 M. A. Kreiger, D. R. Shonnard and J. M. Pearce, Life cycle analysis of silane recycling in amorphous silicon-based solar photovoltaic manufacturing, *Resour., Conserv. Recycl.*, 2013, **70**, 44–49.

29 V. Fthenakis, Sustainability of photovoltaics: The case for thin-film solar cells, *Renewable Sustainable Energy Rev.*, 2009, **13**, 2746–2750.

30 E. Alsema, Energy requirements of thin-film solar cell modules: A review, *Renewable Sustainable Energy Rev.*, 1998, **2**, 387–415.

31 K. Zweibel, Thin film PV manufacturing: Materials costs and their optimization, *Sol. Energy Mater. Sol. Cells*, 2000, **63**, 375–386.

32 C. L. C. McCrory, S. Jung, J. C. Peters and T. F. Jaramillo, Benchmarking heterogeneous electrocatalysts for the oxygen evolution reaction, *J. Am. Chem. Soc.*, 2013, **135**, 16977–16987.

33 E. Kemppainen, A. Bodin, B. Sebok, T. Pedersen, B. Seger, B. Mei, D. Bae, P. C. K. Vesborg, J. Halme, O. Hansen, P. D. Lund and I. Chorkendorff, Scalability and feasibility of photoelectrochemical H_2 evolution: the ultimate limit of Pt nanoparticle as an HER catalyst, *Energy Environ. Sci.*, 2015, **8**, 2991–2999.

34 B. Seger, T. Pedersen, A. B. Laursen, P. C. K. Vesborg, O. Hansen and I. Chorkendorff, Using TiO_2 as a conductive protective layer for photocathodic H_2 evolution, *J. Am. Chem. Soc.*, 2013, **135**, 1057–1064.

35 S. Hu, M. R. Shaner, J. A. Beardslee, M. Lichterman, B. S. Brunschwig and N. S. Lewis, Amorphous TiO_2 coatings stabilize Si, GaAs, and GaP photoanodes for efficient water oxidation, *Science*, 2014, **344**, 1005–1009.

36 *Fuel Cell Technology Handbook*, ed. G. Hoogers, CRC Press, Boca Raton, London, New York, Washington DC, 2003.

37 IPEX, Chemical Resistance Guide: Thermoplastic Piping Systems, 2001.

38 S. M. Rossnagel, Thin film deposition with physical vapor deposition and related technologies, *J. Vac. Sci. Technol., A*, 2003, **21**(5), S74–S87.

39 M. J. Hampden-Smith and T. T. Kodas, Chemical vapor deposition of metals: Part 1: An overview of CVD processes, *Chem. Vap. Deposition*, 1995, **1**, 8–23.

40 R. M. Pasquarelli, D. S. Ginley and R. O'Hayre, Solution processing of transparent conductors: From flask to film, *Chem. Soc. Rev.*, 2011, **40**, 5406–5441.

41 S. J. Kim, S. Yoon and H. J. Kim, Review of solution-processed oxide thin-film transistors, *Jpn. J. Appl. Phys.*, 2014, **53**, 02BA02.

42 C. A. Wolden, J. Kurtin, J. B. Baxter, I. Repins, S. E. Shaheen, J. T. Torvik, A. A. Rockett, V. M. Fthenakis and E. S. Aydil, Photovoltaic manufacturing: Present status, future prospects, and research needs, *J. Vac. Sci. Technol., A*, 2011, **29**, 030801.

43 A. Shah, J. Meier, A. Buechel, U. Kroll, J. Steinhauser, F. Meillaud, H. Schade and D. Domine, Towards very low-cost mass production of thin-film silicon photovoltaic (PV) solar modules on glass, *Thin Solid Films*, 2006, **502**, 292–299.

44 R. J. Hill and S. J. Nadel, *Coated Glass Applications and Markets*, BOC Coating Technology, Fairfield CA, 1999.

45 D. Yue and F. You S.B. Darling, Domestic and overseas manufacturing scenarios of silicon-based photovoltaics:

Life cycle energy and environmental comparative analysis, *Sol. Energy*, 2014, **105**, 669–678.
46 J. Peng, L. Lu and H. Yang, Review on life cycle assessment of energy payback and greenhouse gas emission of solar photovoltaic systems, *Renewable Sustainable Energy Rev.*, 2013, **19**, 255–274.
47 J. Gong, S. B. Darling and F. You, Perovskite photovoltaics: Life-cycle assessment of energy and environmental impacts, *Energy Environ. Sci.*, 2015, **8**, 1953–1968.
48 T. Bronger, P. H. Wöbkenberg, J. Wördenweber, S. Muthmann, U. W. Paetzold and V. Smirnov, *et al.*, Solution-based Silicon in thin film solar cells, *Adv. Energy Mater.*, 2014, **4**, 1301871.
49 National Renewable Energy Laboratory (NREL), *PV-Watts calculator*, 2015. Web-accessed at http://pvwatts.nrel.gov/index.php.
50 National Energy Technology Laboratory (NETL), *Life Cycle Analysis: Power Studies Compilation Report*, National Energy Technology Laboratory Report DOE/NETL-2010/1419, 2010.
51 E. Dahlgren, C. Gocmen, K. Lackner and G. van Ryzin, Small modular infrastructure, *The Engineering Economist*, 2013, **58**, 231–264.
52 E. Worrell, C. Galitsky, E. Masanet and W. Graus, *Energy Efficiency Improvement and Cost Saving Opportunities for the Glass Industry*, Report LBNL-57335, Lawrence Berkeley National Laboratory, 2008.
53 L. L. Gaines and M. M. Mintz, *Energy Implications of Glass-Container Recycling*, Report ANL/ESD-18, Argonne National Laboratory, 1994.
54 J. Johnson, B. K. Reck, T. Wang and T. E. Graedel, The energy benefit of stainless steel recycling, *Energy Policy*, 2008, **36**, 181–192.
55 J. S. Newman and K. E. Thomas-Alyea, *Electrochemical Systems*, Wiley, Hoboken, N.J, 2004.
56 United States Geological Survey (USGS), *Mineral Commodity Summaries*, 2015. http://minerals.usgs.gov/minerals/pubs/commodity/.
57 P. C. K. Vesborg and T. F. Jaramillo, Addressing the terawatt challenge: Scalability in the supply of chemical elements for renewable energy, *RSC Adv.*, 2012, **2**, 7933–7947.
58 American Physical Society (APS) and Materials Research Society (MRS), *Energy Critical Elements: Securing Materials for Emerging Technologies*, 2011. http://www.aps.org/policy/reports/popa-reports/upload/elementsreport.pdf.
59 Y. Chen, C. Xiang, S. Hu and N. S. Lewis, Modeling the performance of an integrated photoelectrolysis system with 10× solar concentrators, *J. Electrochem. Soc.*, 2014, **161**, F1101–F1110.
60 M. Dumortier and S. Haussener, Design guidelines for concentrated photo-electrochemical water splitting devices based on energy and greenhouse gas yield ratios, *Energy Environ. Sci.*, 2015, **8**, 3069–3082.
61 C. C. L. McCrory, S. Jung, I. M. Ferrer, S. M. Chatman, J. C. Peters and T. F. Jaramillo, Benchmarking HER and OER electrocatalysts for solar water splitting devices, *J. Am. Chem. Soc.*, 2015, **137**, 4347–4357.
62 M. Dumortier, S. Tembhurne and S. Haussener, Holistic design guidelines for solar hydrogen production by photo-electrochemical routes, *Energy Environ. Sci.*, 2015, **8**, 3614–3628.

Electronic Supplementary Material (ESI) for Energy & Environmental Science.

Supplementary Information

Opportunities to improve the net energy performance of photoelectrochemical water-splitting technology

Roger Sathre, Jeffery B. Greenblatt, Karl Walczak, Ian D. Sharp, John C. Stevens, Joel W. Ager III, Frances A. Houle

dx.doi.org/10.1039/C5EE03040D

Contents:

S1. Composition and embodied energy of thin film layers

Table S1. Assumed properties and compositions of thin film layers, and resulting specific embodied energy of the elements comprising the layers. A material utilization efficiency (F_m) of 50% is assumed when calculating the specific embodied energy, i.e. half the material is wasted so twice the amount of material in the final film must be sourced. The total specific embodied energy for each film material is summarized in Figure S1.

Film material	Material density	Film thickness	Element	Percent by weight	Embodied energy (per kg)	Embodied energy (per m^2)
	kg/m^3	nm		%	MJ/kg	MJ/m^2
Photoelectrode layers						
InP	4810	250		100%		5.0
			In	79%	2570	4.9
			P	21%	230	0.12
InGaP	4474	250		100%		4.7
			In	47%	2570	2.7
			Ga	28%	3030	1.9
			P	25%	230	0.13
GaAs	5320	250		100%		4.1
			Ga	48%	3030	3.9
			As	52%	140	0.19
WO_3	7160	250		100%		2.3
			W	79%	820	2.3
			O	21%	0	0
a-Si	2330	250	Si	100%	960	1.1
$BiVO_4$	5920	250		100%		2.0
			Bi	65%	700	1.3
			V	16%	1430	0.67
			O	20%	0	0
CdTe	5850	250		100%		0.34
			Cd	47%	70	0.093
			Te	53%	160	0.24
Cu_2O	6000	250		100%		0.092
			Cu	89%	34	0.092
			O	11%	0	0
Fe_2O_3	5745	250		100%		0.046
			Fe	70%	25	0.046
			O	30%	0	0
Catalyst layers						
Pt	21450	1	Pt	100%	263000	11
IrO_x	22420	1	Ir	100%	65000	2.9
NiMo	9594	1		100%		0.0031
			Ni	38%	180	0.0013
			Mo	62%	150	0.0018
$NiFeO_x$	8389	1		100%		0.0019
			Ni	51%	180	0.0017
			Fe	49%	25	0.00019
Fe_3P	6740	1		100%		0.00077
			Fe	84%	25	0.00028

			P	16%	230	0.00048
Fe	7870	1	Fe	100%	25	0.00039
Other layers						
ITO	7140	50		100%		1.4
			In	74%	2570	1.4
			Sn	8%	320	0.02
			O	18%	0	0
FTO	6950	50		100%		0.17
			F	29%	240	0.05
			Sn	56%	320	0.13
			O	15%	0	0
TiO_2	4230	60		100%		0.60
			Ti	60%	1960	0.60
			O	40%	0	0

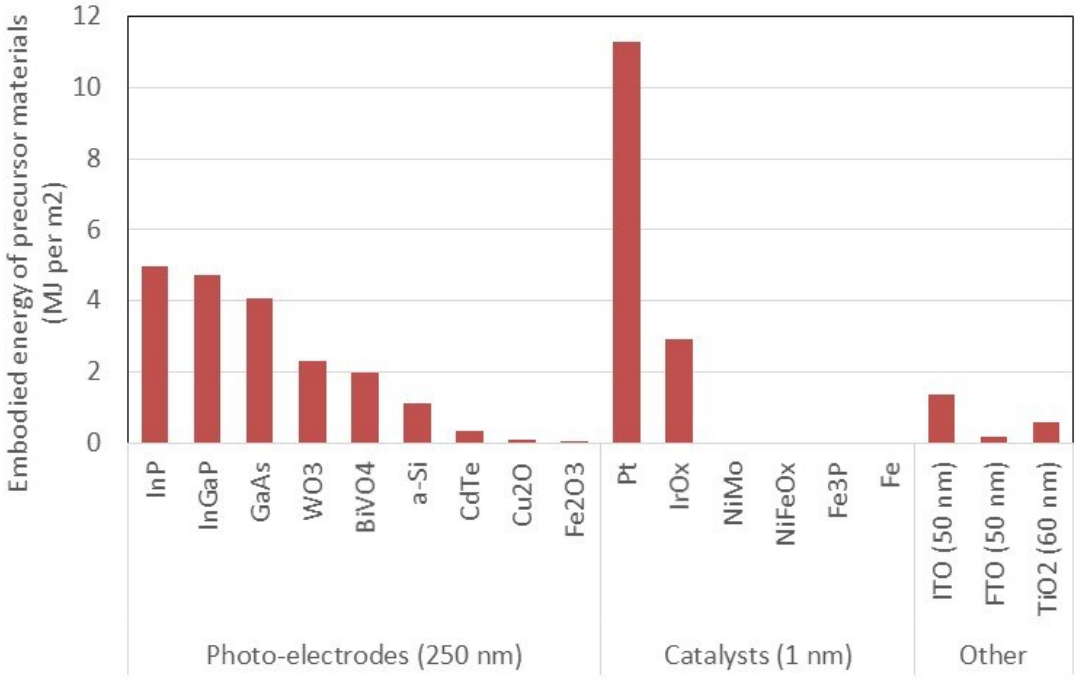

Figure S1. Embodied energy of precursor materials to various types of thin films, per m^2 of coated surface, assuming 50% product yields and 1:1 precursor material energy.

S2. Embodied energy of precursor and final materials

Although standard life cycle inventory (LCI) databases (e.g. Ecoinvent, USLCI) contain embodied energy estimates for thousands of common commodity elements and compounds, they do not include data for tens of thousands of other specialty chemicals that are produced and used in smaller amounts. Robust quantification of the embodied energy of a diverse range of chemical compounds remains a challenge for life cycle assessment practitioners. Many of the final or precursor materials of the thin films studied here (see Section 2.2.1) are not represented in LCI databases or related literature.

There are several approaches to overcoming this knowledge gap. For example, the Finechem tool developed at ETH Zurich[S1] is a software tool to estimate the resource use and environmental impacts of the production of petrochemicals, based on their molecular structure. Ten characteristics of a chemical are entered (e.g. molecular weight, number of nitrogen atoms in the molecule, number of halogen atoms in the molecule, number of aromatic and aliphatic rings in the molecule), and the tool outputs an estimated range of cumulative energy demand for its production, as well as several other life cycle indicators.[S2] However, the range of output values is so broad that the Finechem tool provides little practical utility to LCA practitioners, and is limited to petrochemicals.

Another approach is to survey a selection of proxy materials for which LCI data are available, and use the minimum and maximum values as estimated range of the material of interest. For example, in a prospective life cycle assessment of large-scale production of metal-organic frameworks (MOFs), Sathre & Masanet[S3] estimated the range of energy use for production of MOF organic linker molecules based on proxy data on industrial-scale production of 10 benzene-based organic chemicals. The feedstock energy was found to be the dominant contributor to total energy use for all 10 materials, while the processing and supply chain energy inputs were relatively low. This suggests that the total energy intensity of other potential ligand materials would not differ significantly from this range, because they will have similar feedstock energy. They estimated the range of energy use for MOF metal supply based on data for mining and smelting of elemental metal, as well as proxy data on industrial-scale production of metal salts, e.g. from the fertilizer industry.

Due to the diversity of potential precursor materials used in thin film depositions and the paucity of life cycle inventory data on specialty chemicals, in our modeling we use a simple multiplier expressing the ratio of the embodied energy of precursor materials to the embodied energy of refined elements. In this analysis, many of the materials of interest (Figure S1 and Table S1) are relatively simple metal salt. Figure S2 shows an illustrative example of the embodied energy of two alternate production chains for a desired metallic compound used as a precursor material for thin film deposition. The metallic content of the compound begins as *in situ* ore with zero embodied energy. This ore may then be extracted and processed in various ways, with e.g. mechanical and hydraulic treatment, cumulatively increasing its embodied energy. The ore may be processed through heap leaching, where a reactive solution is repeatedly drained through a pile of ore, and a metal salt is precipitated from the solution. To produce elemental metal, the precipitate is then subject to additional energy intensive processes such as thermochemical refining. The precipitate may, however, be the desired thin film precursor material, or may be transformed into the desired material through minimal additional processing. Alternatively, after refining to elemental metal, the metal may be reacted through various processes to produce the desired metallic compound. This results in two alternate possible ranges for embodied energy of the metallic compound: a value lower than that of refined metal based on production from leachate, and a value higher than that of refined metal based on production and subsequent reaction of refined metal. LCI data are reliably available for refined elemental metals, but are not typically available for specialty metallic compounds. Therefore, and with consideration of Figure S2, we used LCI data on refined metals as our base case embodied energy for precursor materials (based on their content of elemental metal), and apply a multiplier of 2.0 for our high input case, and a multiplier of 0.5 for our low input case. This is the factor

R_p described in Section 2.2.1. These quantitative values are simply assumed, as relevant data are absent in the literature. This topic is ripe for additional research by the LCA community, to develop robust estimates of the embodied energy of a diverse range of chemical feedstocks.

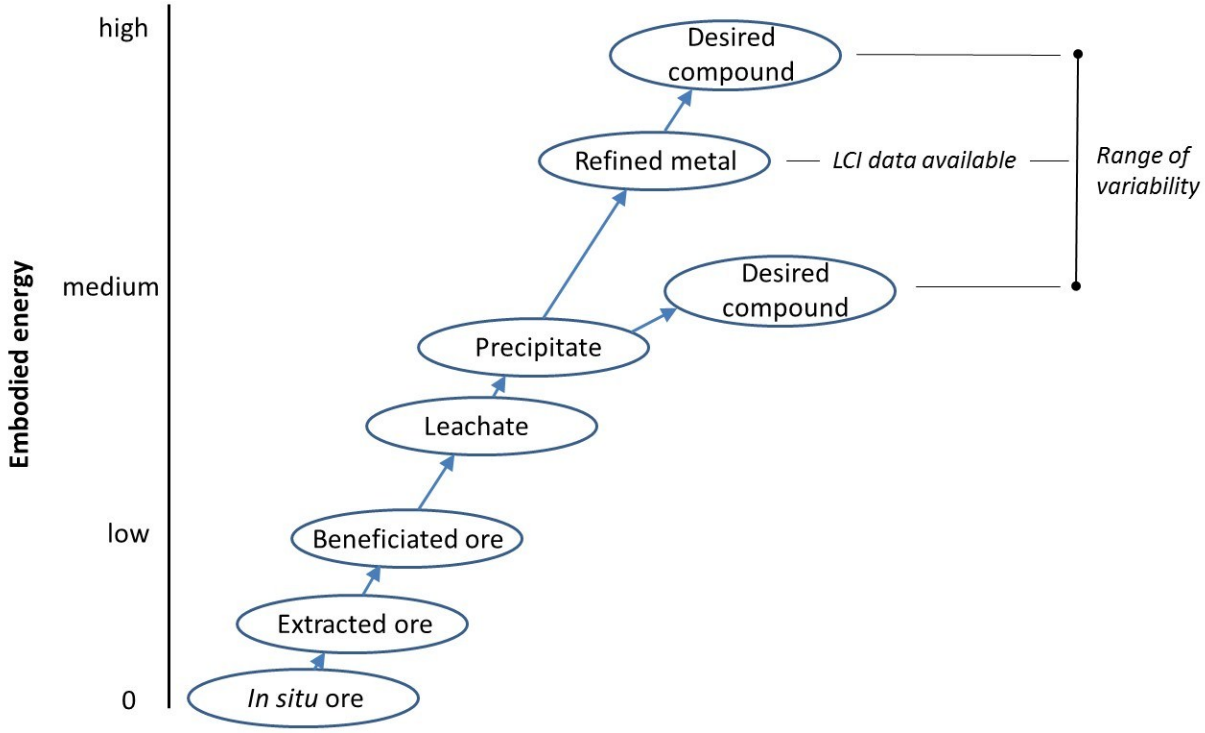

Figure S2. Illustrative example of the embodied energy of alternate production chains of a desired metallic compound.

S3. Encapsulation materials properties and selection

Various materials could be used for the back cover of the PEC module. The selection of materials for the front window is more limited, although at least three light-transmissible materials are available (glass, polycarbonate and poly(methyl methacrylate)). Table S1 shows three properties (density, elastic modulus, and specific embodied energy) of six potential encapsulation materials: flat glass, rigid PVC, polycarbonate, poly(methyl methacrylate), aluminum and stainless steel. The density is lowest for the three polymer materials, highest for the stainless steel, and intermediate for the glass and aluminum. The elastic modulus (also known as Young's modulus) measures the stiffness of the materials, and is quite low for the three plastic materials. The elastic moduli of the glass and aluminum are higher and about the same, while that of stainless steel is highest. The embodied energy of a 2 mm thick sheet of each material ranges from a low of 65 MJ/m^2 for glass, to ~200-300 MJ/m^2 for the two plastic materials, to a high of >1000 MJ/m^2 for the two metals. Since the required thickness of a sheet is inversely proportional to its stiffness, the three plastic materials having low moduli of elasticity would need to be thicker to perform the same structural function as a 2 mm thick sheet of glass or metal. Of all six materials, glass is unique for its relatively high elastic modulus and low embodied energy. Importantly, glass also allows adequate transmissivity of light at wavelengths above 400 nm. For these reasons, and due to its resistance to acidic electrolyte, we choose glass as the most appropriate encapsulation material for PEC modules.

Table S2. Properties of six potential encapsulation materials for PEC modules.

Material	Density	Elastic modulus	Specific embodied energy of 2 mm thick sheet
	g/cm^3	*Gpa*	*MJ/m^2*
Float glass	2.5	~70	65
Rigid PVC	1.4	~3	170
Polycarbonate	1.2	~2.2	260
Poly(methyl methacrylate)	1.2	~2.6	340
Aluminum	2.7	~70	1050
Stainless Steel	7.9	~180	1230

The elastic modulus is a useful indicator of stiffness, although the overall "strength" of glass depends on several properties and cannot be expressed as a single number. It can, however, be characterized. For instance, Veer[S4] performed a set of experimental 3- and 4-point bending tests, with high numbers of repetitions on different thicknesses of glass, and generally found that glass fails at ~50-70 MPa for 2 mm thick plates (area dimensions 400x40 mm), but thicker plates—up to 8 mm—failed at roughly the same pressure. It is therefore clear that thickness alone does not determine resistance to breakage; surface defects are just as, if not more, important. Tempered, annealed and heat-treated glasses have reduced numbers of defects, thus increasing strength.

Standards exist for the types of glasses used in windows and other structural applications, generally referred to as "architectural" glass. These standards are based primarily on two performance characteristics: the maximum three-second wind gust and the maximum hailstone impact energy, and are both driven by glass thickness and, to a lesser extent, the type of heat treatment.

According to maps of US three-second maximum gust wind speeds (e.g.[S5]), ≥90 mph winds only occur near shorelines on the Gulf of Mexico and southern Atlantic Ocean, areas that are prone to hurricanes. For all other areas in the US, the maximum three-second gust wind speed is <90 mph. This corresponds to a design pressure (DP) rating of DP-20.[S6]

Cardinal Glass[S7,S8] provides thickness guides for glass usage. The lowest rating provided is DP-30, which recommends 2.2 mm thickness for heat-treated glass with 15 ft^2 (~1.4 m^2) spanned area and maximum length of 6 ft. (~1.8 m); for 20 ft^2 (~1.9 m^2), the recommended thickness is 3 mm. Annealed glass has somewhat more conservative requirements. The DP-20 ratings may be more lenient; however, we have assumed the DP-30 requirements for our analysis, limiting module sizes to ≤1.4 m^2 and ≤1.8 m on its longest side for 2 mm thickness. Furthermore, considering that our module uses two panes of glass rigidly connected by the PVC supporting ribs, we could then consider the total thickness instead of the individual pane thickness. In this case, 4 mm total thickness has a maximum span area of 30 ft^2 = 2.8 m^2 for heat-treated glass, which is more than adequate for our module size.

While the average glass thickness used by the PV industry ranges from ~2 to 6 mm,[S9] recent advances in process optimization have allowed some companies (e.g.[S10]) to reduce their maximum thicknesses from a "typical" 3 mm thickness for solar PV modules[S11] to 2.3-2.6 mm.

For hail, SolarWorld[S12] reports an impact test that "replicates a natural hail storm by dropping a 1.1-pound, one-inch steel ball onto solar panels from a height of 13 feet." This translates to an impact energy of 14.3 ft-lbs. (~19 J), equivalent to FM Class I-SH test hailstone of 45 mm (~1.75 inch) diameter. This is similar to testing for roofing materials.[S13] According to a US hail damage report,[S14] hail events are concentrated in the Great Plains region of the country, with a 50% risk of 1-inch (2.54 cm) or larger hailstones occurring at least once in five years. Probability drops off quickly outside this region. In areas where we expect most PEC systems to be located, e.g. high-insolation regions in the US desert southwest, the probability of large hail storms is extremely remote. A separate map of average hailstone diameter is similarly concentrated in the Great Plains, where it exceeds one inch (2.54 cm). In Arizona and New Mexico, the average diameter follows a strong gradient, ranging from <0.2 inch (<0.51 cm) in the west to 1.0 inch (2.54 cm) at the extreme eastern edge. This band of low-diameter hail extends upward into California and Nevada as well.

S4. Module frame design

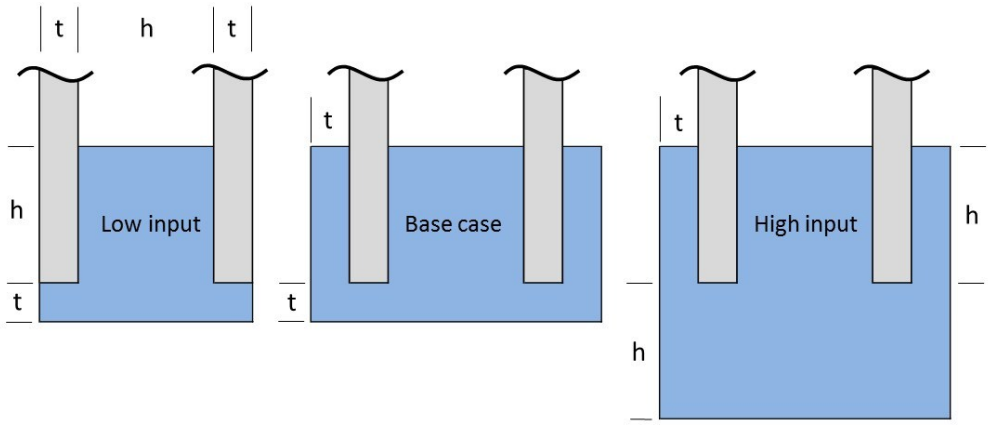

Figure S3. Dimensions of three alternative designs of PEC module frame, each made of PVC. The dimension "t" is the thickness of the glass window and back cover, and "h" is the inside dimension of the module enclosure.

S5. Panel structural design

We perform an initial structural design of the panels, based on calculations of deflection under load. Considering the panel as a uniformly-loaded beam that is simply supported at three points (Figure S4, left), symmetry implies that deflection will be equal to a beam fixed on one end and simply supported on the other (Figure S4, right).

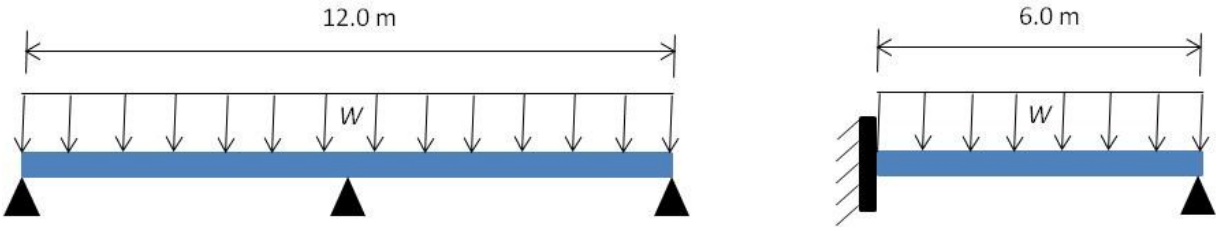

Figure S4. Estimation of panel deflection under load.

Based on Pope[S15], maximum deflection (inches) for a beam fixed on one end and simply supported on the other will be:

$$y_{max} = \frac{-0.0054\, W\, L^4}{E\, I}$$

where W is the uniform load (pounds inch^{-1}), L is the length of the beam (inch), E is the modulus of elasticity of the material (psi), and I is the moment of inertia of the beam (inch^4). In this deflection analysis we assume the panel is lying flat; the uniform load is composed of the dead load of the steel structure (1.0 pounds inch^{-1}) plus the load of the PEC components and electrolyte (2.2 pounds inch^{-1}), to which is applied a safety factor multiplier of 3. The length of the (half) panel is 6.0 m or 237 inches. The modulus of elasticity of steel is about 3.1x10^7 psi. A cross section of the panel structural frame member is shown in Figure S5. The moment of inertia of this section is 2.43 inch^4; this quantity is then doubled because the perimeter frame has two members. These properties yield a maximum calculated deflection of about 1.0 inch. The calculated length-to-deflection ratio is about 220, which is marginally acceptable for typical structural applications.

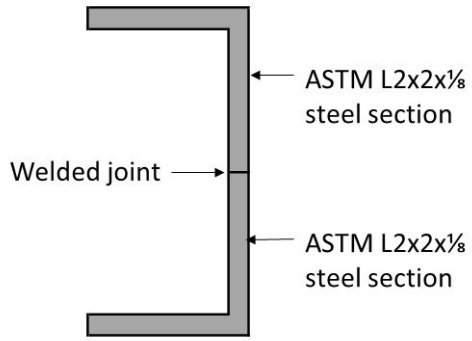

Figure S5. Cross section of panel perimeter structural frame.

The panel perimeter structural frame (Figure S5) is composed of 2 separate structural steel sections welded together, thus providing the same structural integrity with less material use compared to our earlier solutions employing a single larger steel section (Sathre et al. 2014). Although an improvement, this solution continues the use of "off the shelf" components for panel manufacture, which is appropriate for small-scale implementation of the technology. If PEC water splitting technology is to scale up as

modeled in this analysis (employing almost 1.6 million individual panels per 1 GW facility), a much more rigorous structural optimization process is likely to be conducted, resulting in a more efficient structural solution using less steel material. Such optimization is analogous to the transition from traditional "body-on-frame" designs used previously by the automobile industry, to the more efficient "unibody" designs now used overwhelmingly in vehicles. MacKenzie et al.[S16] report that the switch to unibody car design has resulted in a weight reduction of 18.5% on average. We expect there is still scope for further panel material reductions if similar structural optimization process is employed for large-scale PEC panel manufacture.

S6. Facility location and solar insolation

In our main analysis we consider the average solar insolation at four sites in the southwest US: Phoenix, Daggett, Tucson, and Las Vegas. Solar resource data are the average of monthly mean insolation on flat panels oriented south and tilted at the angle of latitude. In a sensitivity analysis, we also consider insolation data from a more representative selection of US sites: Charlotte, Omaha, Salt Lake City and Chicago. Details on solar insolation at each site are shown in Figure S6.

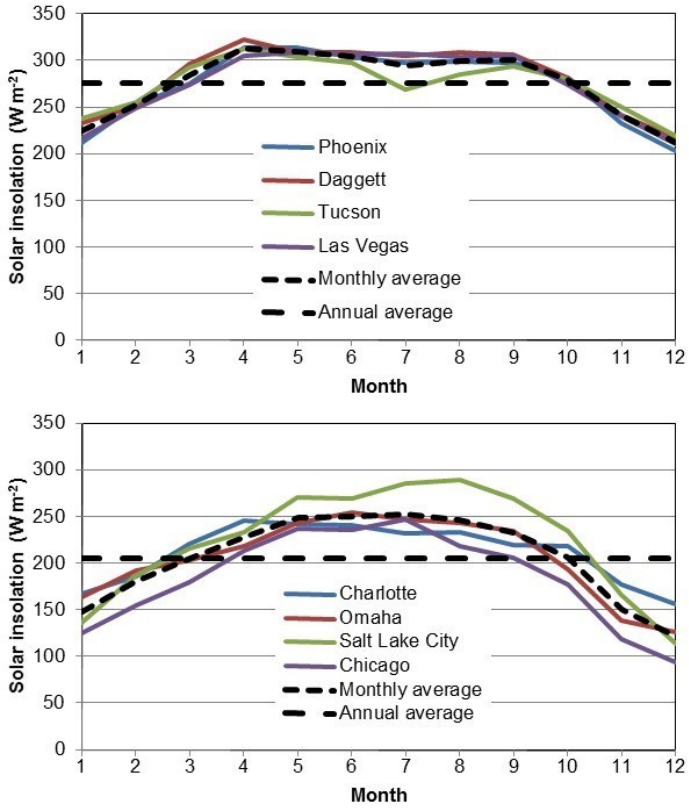

Figure S6. Solar insolation data for four US southwest locations used in our base-case analysis (top), and for four US north-central locations used in a sensitivity analysis (bottom).

S7. Monte Carlo simulation of balance-of-system energy use

The balance of system (BOS) is characterized by a series of parameters describing aspects of panels, piping, gas handling, gas storage, water supply, roads, and facility operations. Each parameter is defined by a base-case value, a high energy input value, and a low energy input value (see Table S3).

Table S3. Parameter values describing the balance of system (BOS)

Parameter description	Units	High input	Base case	Low input
Panel				
Panel inactive area	percent	15%	10%	5%
Panel material use	multiplier	1.2	1.0	0.8
Panel material energy intensity	multiplier	1.2	1.0	0.8
Panel internal frame spacing	meter	0.5	1.0	1.5
Panel transport (truck and train)	kilometer	1300	300	0
Containment vessel thickness	meter	0.008	0.004	0.002
Containment vessel material energy	multiplier	1.5	1.0	0.8
Piping				
Maximum velocity, uncompressed H_2	m sec^{-1}	0.5	1.0	2.0
Maximum velocity, compressed H_2	m sec^{-1}	20	40	60
Maximum velocity, H_2O	m sec^{-1}	1.0	3.0	5.0
Material energy intensity	multiplier	1.2	1.0	0.8
Allowance for valves and fittings	percent	50%	25%	10%
Pipe transport (train)	kilometer	3000	1000	300
Gas handling				
Panels per blower	units	50	100	150
Gas blower power	kW	3.0	1.5	0.7
Gas blower average use	percent of capacity	100%	75%	50%
Gas dryer power	kW	5.0	2.4	1.4
Gas dryer average use	percent of capacity	100%	75%	50%
Compressor specific energy use	W h m^{-3}	82	70	57
Compressor interstage loss	psi	10	5	0
Gas intake temperature	degree C	80	60	40
Compressor fan load	percent	10%	7.5%	5%
Gas handling hardware embodied energy	multiplier	2.0	1.0	0.5
Storage				
Gas storage capacity	day	2.0	1.0	0.5
Allowable stress in tank wall	multiplier	0.8	1.0	1.2
Corrosion allowance	mm	12	9	6
Allowance for valves and fittings	percent	20%	10%	5%
Water				
Water treatment electricity	MJ ton^{-1} of treated water	43.1	21.5	16.1
Water treatment brine waste	liter ton^{-1} of treated water	774	387	71
Water use for panel cleaning	liter m^{-2} $year^{-1}$	100	25	10
Water transport electricity	kWh m^{-3} km^{-1}	0.0073	0.0047	0.0018
Roads				
Road width	meter	8	6	4
Asphalt thickness	meter	0.10	0.05	0.03
Subbase thickness	meter	0.30	0.15	0.08
Percent bitumen in asphalt	percent	6%	5%	4%
Material energy intensity	multiplier	1.2	1.0	0.8
Operations				
Number of trucks and cranes	units	12	6	3
Horsepower of engines	brake hp	600	400	200
Daily operating time	hours	24	12	8

Equipment load factor	ratio	0.70	0.54	0.38
Panel heat requirement	kWh m^{-2} $year^{-1}$	11.1	5.4	0.5

We use Monte Carlo simulations to estimate uncertainty introduced by interactions between multiple individual parameters describing the BOS. Simulation was conducted using Oracle® Crystal Ball software. Triangular probability distributions were assumed for each parameter based on low input, base-case and high input values (Table S3). A triangular distribution is defined by three points: the minimum, most likely, and maximum values. The high and low parameter values used in our study are selected as likely absolute minimums and maximums, and are thus well suited to a triangular distribution. Based on the outcome distribution of 10,000 simulations with simultaneous variation of each variable, the mean values of initial and continuing BOS energy inputs are used as base-case parameter values, and 90% confidence intervals are used as high input and low input parameter values. Because the BOS requirements of a fixed-output facility will depend on STH efficiency and cell life span, we conducted nine separate simulations considering each combination of these parameters. Outcomes are shown in Figure S6.

Figure S7. Outcomes of Monte Carlo simulations of BOS energy use, for nine combinations of STH efficiency and cell life span.

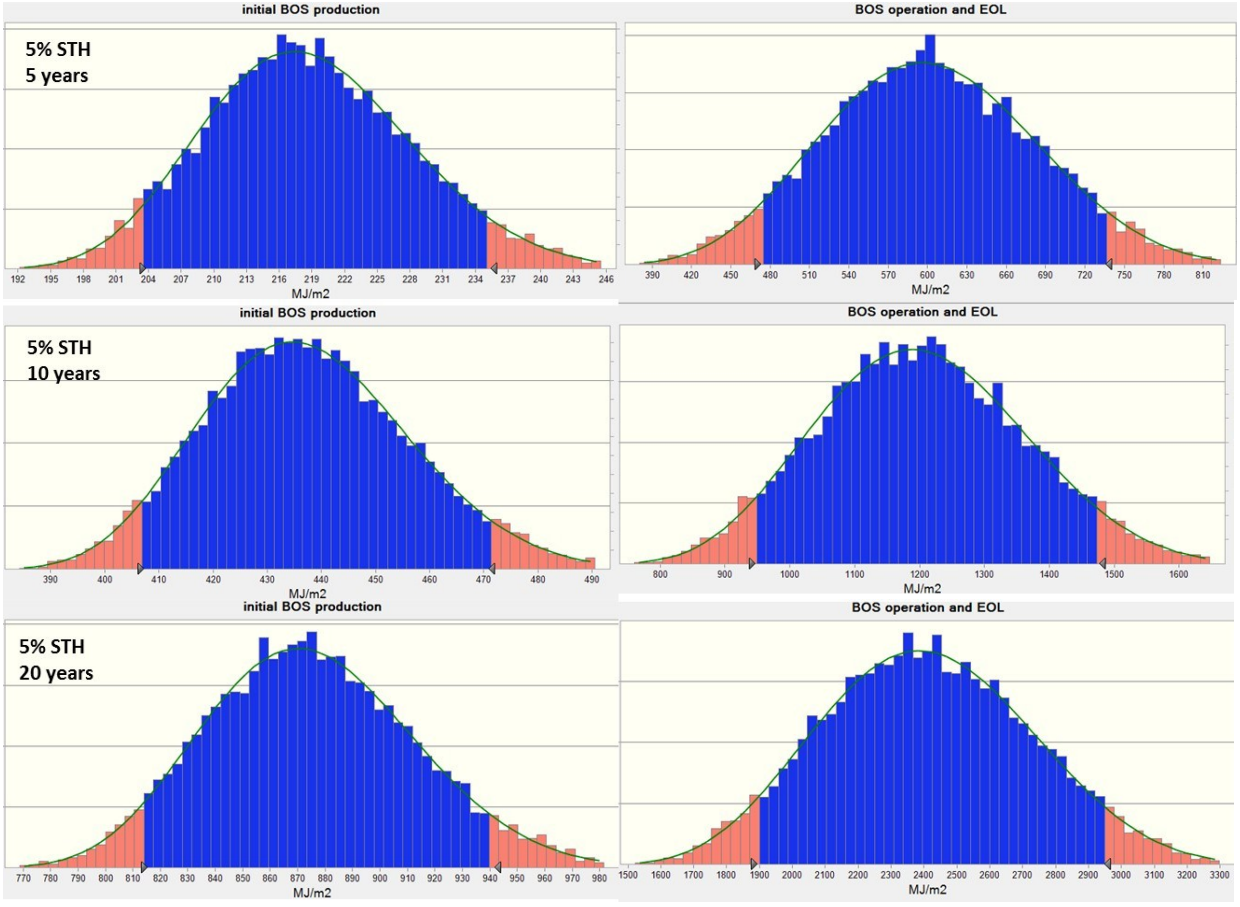

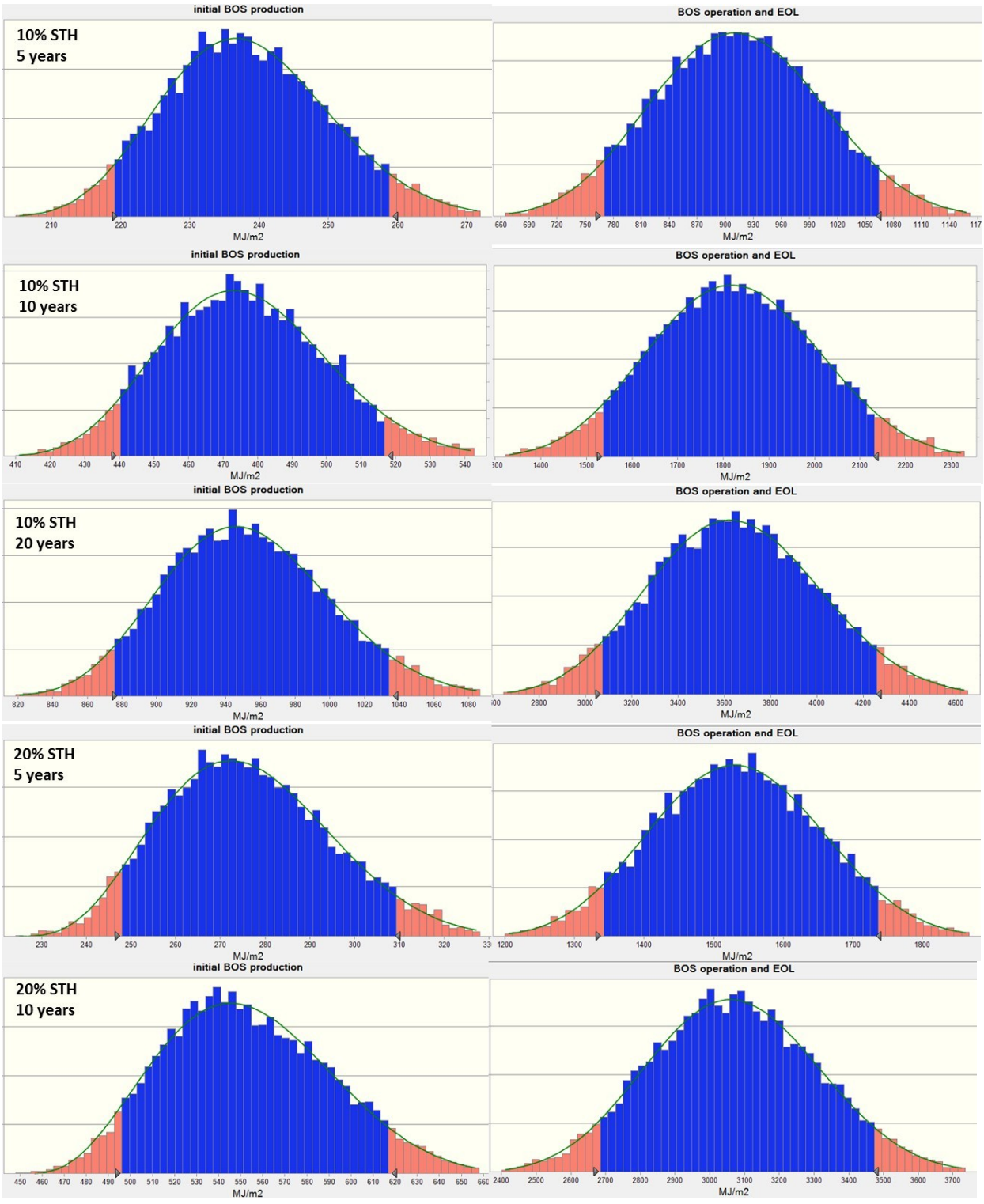
initial BOS production
10% STH
5 years
210 220 230 240 250 260 270
MJ/m2
BOS operation and EOL
660 690 720 750 780 810 840 870 900 930 960 990 1020 1050 1080 1110 1140 117
MJ/m2
initial BOS production
10% STH
10 years
410 420 430 440 450 460 470 480 490 500 510 520 530 540
MJ/m2
BOS operation and EOL
300 1400 1500 1600 1700 1800 1900 2000 2100 2200 2300
MJ/m2
initial BOS production
10% STH
20 years
820 840 860 880 900 920 940 960 980 1000 1020 1040 1060 1080
MJ/m2
BOS operation and EOL
00 2800 3000 3200 3400 3600 3800 4000 4200 4400 4600
MJ/m2
initial BOS production
20% STH
5 years
230 240 250 260 270 280 290 300 310 320 33
MJ/m2
BOS operation and EOL
1200 1300 1400 1500 1600 1700 1800
MJ/m2
initial BOS production
20% STH
10 years
450 460 470 480 490 500 510 520 530 540 550 560 570 580 590 600 610 620 630 640 650 660
MJ/m2
BOS operation and EOL
2400 2500 2600 2700 2800 2900 3000 3100 3200 3300 3400 3500 3600 3700
MJ/m2

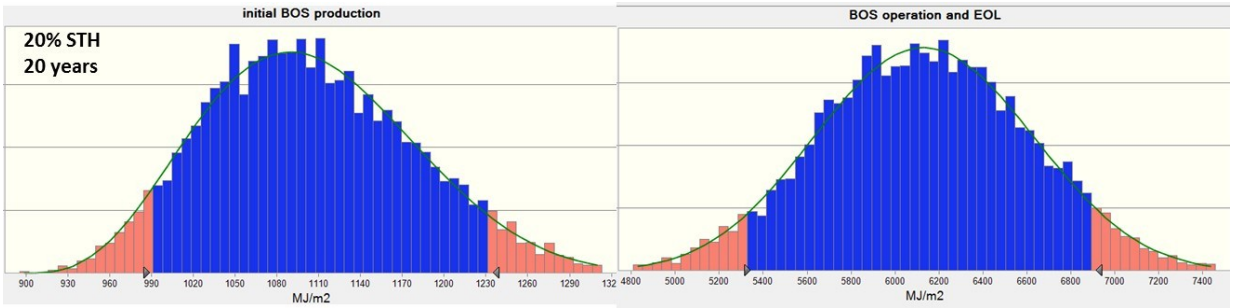
initial BOS production
20% STH
20 years
900 930 960 990 1020 1050 1080 1110 1140 1170 1200 1230 1260 1290 132
MJ/m2
BOS operation and EOL
4800 5000 5200 5400 5600 5800 6000 6200 6400 6600 6800 7000 7200 7400
MJ/m2

S8. Module heating to avoid freezing

Per the analysis described by Sathre et al.[S17], heating of modules may be required to prevent freezing of the electrolyte during cold weather. The freezing temperature of 1 molar sulfuric acid is approximately -5 °C. If the PEC cells drop below this temperature, they will freeze, potentially rupture, and fail. To prevent freezing, the underside of each module could be fitted with an electrically powered strip heater to provide heating when the embedded temperature sensors determine this necessary. This heater can also be backed by a layer of insulation. We used a computational model to assess the degree of heating required for the modules, to estimate its effect on the facility's net energy production. Given the small aspect ratio of the modules (thickness divided by length or width), a one-dimension finite-difference transient heat transfer model was constructed, with coupled heat transfer equations solved for each hour of the year for the top window, anolyte, light absorber assembly, catholyte, case backing, strip heater and (when applicable) insulation layers. It was assumed that the modules only transfer heat out to the environment via radiation and convection. These modules would heat up in the daytime due to the conversion of insolation into waste heat in the light absorber assembly and in the semitransparent top window; joule heating of the electrolyte was ignored given the low current densities of this device. If the temperature of the device dropped below a temperature threshold of -2.5 °C, a one-dimension steady-state heat transfer model was used to estimate the required heater energy input to prevent the electrolyte temperature from dropping further. This minimum temperature threshold is greater than the electrolyte freezing temperature to provide an operational safety margin.

In our earlier analysis[S17], we estimated the total annual electricity requirement for heating. This varied between the four selected sites in the US southwest, with Daggett requiring the most at 11.0 kWh m^{-2} yr^{-1}, and Phoenix needing the least at 0.6 kWh m^{-2} yr^{-1}. The average of the sites is 5.4 kWh m^{-2} yr^{-1}, which we adopt as our base-case heating requirement. Although the internal convection coefficients of the louvered design are different from the previous micro-wire system, resultant from the changes to the internal cell geometry, we assume this will not change the heating energy needs.

S9. Hydrogen demand scale-up scenarios

We conduct a scale-up analysis to estimate required quantities of thin film materials and identify potential constraints in material availability. We consider three hydrogen demand scale-up scenarios of varying extent: Use of hydrogen fuel in 10% of the US passenger car and light truck fleet would require 14 facilities producing 1 GW (continuous annual average) each. Use of hydrogen fuel in 100% of the US light vehicle fleet through 2040 would require 142 1 GW facilities. Global scale-up through 2040 to cover the demand of all light duty vehicles is projected to require 850 facilities of 1 GW each.

US light-duty vehicle travel demand in 2040 is estimated to be 3.57 trillion miles.[S18] Based on NAS[S19], we assume that by 2040 average light-duty vehicle hydrogen fuel cell efficiency will be 8.8 kg H_2 per 1000 miles (based on the average of passenger car and light truck efficiencies), roughly five times more efficient than current conventional gasoline engines. This results in an annual demand of 31.4 billion kg H_2 in 2040. Since each 1 GW facility produces 222 million kg H_2 per year, about 142 such facilities would be required to fully meet US demand. If 10% of US vehicles were hydrogen-powered, about 14 facilities would be required. Extrapolating globally, demand for petroleum for transportation in 2040 is projected to be roughly six times that in the US. Assuming this applies to light-duty vehicle demand, and that all vehicles are hydrogen-powered in 2040, approximately 850 1 GW plants would be required globally.

The total PEC cell area required is based on 10% STH efficiency, with annual material requirements based on a 10-year cell life span. Our calculations use our base-case value of 50% material utilization efficiency in thin film deposition, which assumes that half of the material is deposited on the substrate and the other half is wasted (material utilization efficiency is discussed in Section 2.2.1). Waste recovery efforts would likely be employed for high value materials, thus we likely overestimate the consumption of such materials. Results are summarized in Figure S7, and detailed in Table S4.

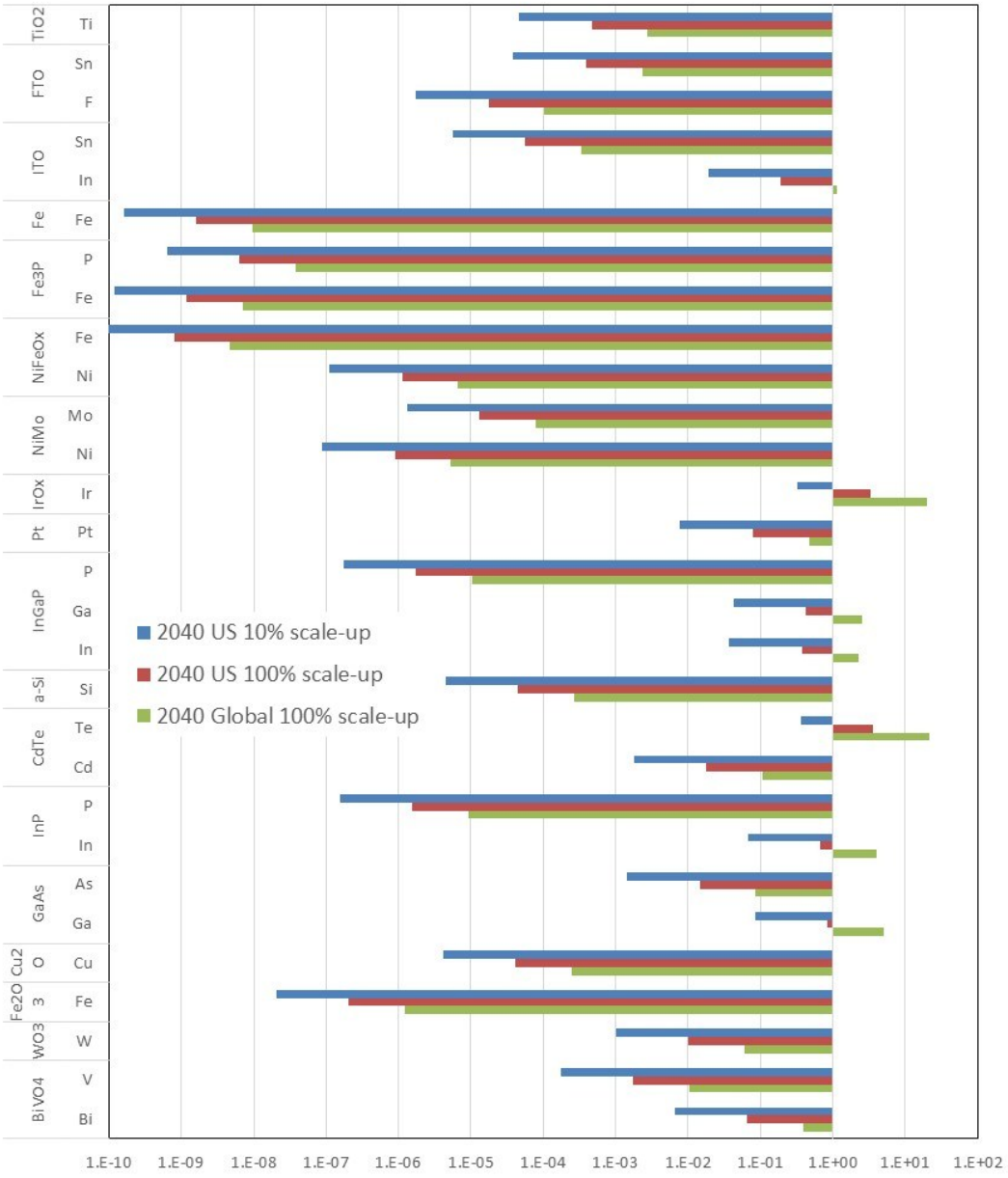

Figure S8. Amount of thin film materials needed for PEC hydrogen production at 3 scale-up levels, expressed as proportion of 2014 global primary production (i.e., 1 is 100% of 2014 production, 0.1 is 10% of 2014 production, etc.).

Table S4. Amount of thin film materials needed for PEC hydrogen production, expressed as tons of materials contained in an operating 1GW facility, tons of materials needed annually for three scale-up levels, and percentage of 2014 global primary production for three scale-up levels.

			Tons per year needed			Percent of 2014 mine production		
Thin film material	Element	Tons per facility	2040 US 10% scale-up	2040 US 100% scale-up	2040 Global 100% scale-up	2040 US 10% scale-up	2040 US 100% scale-up	2040 Global 100% scale-up
Photoelectrode layers (250 nm)								
$BiVO_4$	Bi	39.4	56	560	3351	0.66%	6.6%	39%
	V	9.6	14	136	817	0.02%	0.17%	1.0%
WO_3	W	58.6	83	832	4982	0.10%	1.0%	6.0%
Fe_2O_3	Fe	41.5	59	589	3526	<0.001%	<0.001%	<0.001%
Cu_2O	Cu	55.0	78	781	4676	<0.001%	0.004%	0.025%
GaAs	Ga	26.5	38	376	2250	8.5%	85%	510%
	As	28.4	40	404	2418	0.14%	1.4%	8.6%
InP	In	39.1	56	555	3324	6.8%	68%	400%
	P	10.5	15	150	897	<0.001%	<0.001%	0.001%
CdTe	Cd	28.3	40	402	2404	0.18%	1.8%	11%
	Te	32.1	46	456	2729	36%	370%	2200%
a-Si	Si	24.1	34	342	2045	<0.001%	0.004%	0.027%
InGaP	In	21.5	31	306	1829	3.7%	37%	220%
	Ga	13.1	19	186	1111	4.2%	42%	250%
	P	11.6	16	165	987	<0.001%	<0.001%	0.001%
Catalyst layers (1 nm)								
Pt	Pt	0.89	1.3	13	75	0.78%	7.8%	47%
IrOx	Ir	0.93	1.3	13	79	33%	330%	1970%
NiMo	Ni	0.15	0.2	2.1	13	<0.001%	<0.001%	0.001%
	Mo	0.25	0.35	3.5	21	<0.001%	0.001%	0.008%
NiFeOx	Ni	0.19	0.27	2.7	16	<0.001%	<0.001%	0.001%
	Fe	0.16	0.23	2.3	13	<0.001%	<0.001%	<0.001%
Fe_3P	Fe	0.23	0.33	3.3	20	<0.001%	<0.001%	<0.001%
	P	0.04	0.062	0.6	3.7	<0.001%	<0.001%	<0.001%
Fe	Fe	0.32	0.46	4.6	28	<0.001%	<0.001%	<0.001%
Other layers								
ITO (200 nm)	In	11.0	16	156	933	1.9%	19%	114%
	Sn	1.2	1.6	16	99	<0.001%	0.006%	0.033%
FTO (200 nm)	F	4.1	6	58	348	<0.001%	0.002%	0.010%
	Sn	8.1	11	115	686	0.004%	0.039%	0.23%
TiO_2 (60 nm)	Ti	6.3	9	89	534	0.005%	0.047%	0.28%

S10. Additional references used in the Supplementary Information

S1 ETH Zurich, *The Finechem Tool*, 2010. http://www.sust-chem.ethz.ch/tools/finechem.

S2 G. Wernet, S. Papadokonstantakis, S. Hellweg and K. Hungerbuhler, Bridging data gaps in environmental assessments: Modeling impacts of fine and basic chemical production, *Green Chem*., 2009, 11, 1826–1831.

S3 R. Sathre and E. Masanet, Long-term energy and climate implications of carbon capture and storage deployment strategies in the US coal-fired electricity fleet. *Environmental Science & Technology*, 2012, **46**, 9768–9776.

S4 F.A. Veer, The strength of glass, a nontransparent value, *Heron Journal*, 2007. http://heronjournal.nl/52-12/4.pdf

S5 WindSpeedByZip, *Wind Speed By Zip*, 2015. http://www.windspeedbyzip.com/

S6 National Certified Testing Laboratories, *Wind Velocity Chart*, 2015. http://www.nctlinc.com/velocity-chart/

S7 Cardinal IG Company, *Glass Windload Tables*, Technical service bulletin #IG03, 2008. http://www.cardinalcorp.com/wp-content/uploads/pdf/tsb/ig/IG03_05-08.pdf;

S8 Cardinal IG Company, *Technical Glass Guide, Version 2.0*, 2014. http://www.cardinalcorp.com/wp-content/uploads/pdf/Technical_Glass_Guide_Web.pdf

S9 PPG, *Solarphire™ PV High-Transmissive Glass*, 2010. http://www.ppg.com/en/solutionbyindustry/energy/solar/documents/finalsolarphirepvproductdatasheet.pdf

S10 PV Tech, *Centrosolar Glas offers 30% reduction of module glass thickness and weight*, 2012. http://www.pv-tech.org/product_reviews/centrosolar_glas_offers_30_reduction_of_module_glass_thickness_and_weight

S11 Green Rhino Energy, *Solar Glass & Mirrors* , 2013. http://www.greenrhinoenergy.com/solar/technologies/solar_glass.php

S12 SolarWorld Americas, *The SolarWorld Standard* , 2015. http://www.solarworld-usa.com/why-choose-solarworld/the-solarworld-standard

S13 V. Crenshaw and J.D. Koontz, *Simulated Hail Damage and Impact Resistance Test Procedures for Roof Coverings and Membranes*, 2000. http://jdkoontz.com/articles/simulated.pdf

S14 S.A. Chagnon, D. Chagnon and S.D. Hilbert, *Hailstorms across the Nation: An Atlas about Hail and Its Damages*, Illinois State Water Survey, Contract Report 2009-12, 2009. http://www.isws.illinois.edu/pubdoc/CR/ISWSCR2009-12.pdf

S15 J.E. Pope, *Rules of Thumb for Mechanical Engineers*, Gulf Publishing Company, Houston, 1997.

S16 D. MacKenzie, S. Zoepf and J. Heywood, Determinants of US passenger car weight, *Int. J. of Vehicle Design*, 2014, **65**, 73-93.

S17 R. Sathre, C.D. Scown, W.R. Morrow, J.C. Stevens, I.D. Sharp, J.W. Ager, K. Walczak, F.A. Houle and J.B. Greenblatt, Life-cycle net energy assessment of large-scale hydrogen production via photoelectrochemical water splitting, *Energy Environ. Sci*., 2014, **7**: 3264-3278.

S18 Energy Information Administration (EIA), *Annual Energy Outlook 2015*, US Department of Energy, 2015. http://www.eia.gov/forecasts/aeo/.

S19 National Academies of Science (NAS), *Transitions to Alternative Vehicles and Fuels*, The National Academies Press, Washington DC, 2013. http://www.nap.edu/catalog.php?record_id=18264.